

AD \_\_\_\_\_

Award Number: DAMD17-99-1-9429

TITLE: Automatic Exposure Control Device for Digital Mammography

PRINCIPAL INVESTIGATOR: Laurie L. Fajardo, M.D.

CONTRACTING ORGANIZATION: The University of Iowa  
Iowa city, Iowa 52242

REPORT DATE: August 2004

TYPE OF REPORT: Final

PREPARED FOR: U.S. Army Medical Research and Materiel Command  
Fort Detrick, Maryland 21702-5012

DISTRIBUTION STATEMENT: Approved for Public Release;  
Distribution Unlimited

The views, opinions and/or findings contained in this report are those of the author(s) and should not be construed as an official Department of the Army position, policy or decision unless so designated by other documentation.

**REPORT DOCUMENTATION PAGE**Form Approved  
OMB No. 074-0188

Public reporting burden for this collection of information is estimated to average 1 hour per response, including the time for reviewing instructions, searching existing data sources, gathering and maintaining the data needed, and completing and reviewing this collection of information. Send comments regarding this burden estimate or any other aspect of this collection of information, including suggestions for reducing this burden to Washington Headquarters Services, Directorate for Information Operations and Reports, 1215 Jefferson Davis Highway, Suite 1204, Arlington, VA 22202-4302, and to the Office of Management and Budget, Paperwork Reduction Project (0704-0188), Washington, DC 20503

<b>1. AGENCY USE ONLY</b> (Leave blank)		<b>2. REPORT DATE</b> August 2004	<b>3. REPORT TYPE AND DATES COVERED</b> Final (1 Aug 99 - 30 Aug 04)	
<b>4. TITLE AND SUBTITLE</b>  Automatic Exposure Control Device for Digital Mammography			<b>5. FUNDING NUMBERS</b> DAMD17-99-1-9429	
<b>6. AUTHOR(S)</b> Laurie L. Fajardo, M.D.				
<b>7. PERFORMING ORGANIZATION NAME(S) AND ADDRESS(ES)</b> The University of Iowa Iowa city, Iowa 52242  E-Mail:			<b>8. PERFORMING ORGANIZATION REPORT NUMBER</b>	
<b>9. SPONSORING / MONITORING AGENCY NAME(S) AND ADDRESS(ES)</b> U.S. Army Medical Research and Materiel Command Fort Detrick, Maryland 21702-5012			<b>10. SPONSORING / MONITORING AGENCY REPORT NUMBER</b>	
<b>11. SUPPLEMENTARY NOTES</b>  Report contains color				
<b>12a. DISTRIBUTION / AVAILABILITY STATEMENT</b> Approved for Public Release; Distribution Unlimited				<b>12b. DISTRIBUTION CODE</b>
<b>13. ABSTRACT (Maximum 200 Words)</b>  None Provided				
<b>14. SUBJECT TERMS</b>  Digital mammography, breast cancer, automatic exposure device				<b>15. NUMBER OF PAGES</b> 48
				<b>16. PRICE CODE</b>
<b>17. SECURITY CLASSIFICATION OF REPORT</b> Unclassified	<b>18. SECURITY CLASSIFICATION OF THIS PAGE</b> Unclassified	<b>19. SECURITY CLASSIFICATION OF ABSTRACT</b> Unclassified		<b>20. LIMITATION OF ABSTRACT</b> Unlimited

NSN 7540-01-280-5500

Standard Form 298 (Rev. 2-89)  
Prescribed by ANSI Std. Z39-18  
298-102

## Table of Contents

Cover.....	1
SF 298.....	2
Table of Contents.....	3
Introduction.....	4
Body.....	4
Key Research Accomplishments.....	20
Reportable Outcomes.....	23
Conclusions.....	23
References.....	25
Appendices.....	25



## Introduction

The broad, long-term objective of this IDEA proposal is to achieve optimized image quality for DM within acceptable limits of radiation exposure by developing innovative approaches for controlling DM exposures. These approaches entail using the digital detector and an artificial neural network to control mammographic exposures. This project's specific aims are (1) to use short, low dose pre-exposures of the breast to create "intelligent" regions of interest that determine the exposure parameters for the fully exposed image; and (2) to use an artificial neural network to select exposure parameters (mAs, kVp, and beam filtration) based on "intelligent decisions" that optimize signal-to-noise (SNR) as a function of mean glandular dose.

## Body: Progress on Research Tasks & Key Research Accomplishments

### **Task 1. Determine optimal pixel binning factor and size of exposure-controlling ROI.**

The ideal exposure-controlling ROI (ECROI) is large enough so that small, high-density structures such as calcifications are not selected to determine exposure parameters, but small enough so that the image is not smoothed excessively. To determine an optimal ECROI size, we surveyed FFDM images from our clinical image database, evaluating 3-D surface plots to determine where the "peaks" of low exposure areas are located and the range of the super-pixel values in the peaks. This provided information on the effects of the location and size of the ECROI. We evaluated the effect of the ECROI size on the calculation of the SNR (Figures 1-7). Next, we developed software to analyze selected ROIs (super-pixels) of digitally acquired mammograms. The primary two questions to be addressed by these analysis tools are:

- 1) Which area of the digitally obtained mammogram contains the area of greatest radiographic attenuation (the ECROI)?
- 2) What portion of the pixel variance in the ECROI is a result of differential breast attenuation (signal) as opposed to random fluctuations (noise)?

With respect to question 1), the immediate objectives of the software programs are:

- a) Evaluate the correlation between the number of regions of interest (ROIs) sampled and the correct identification of the ROI containing the area of greatest radiographic attenuation (the ECROI)
- b) Evaluate the correlation between ROI size and correct identification of the ECROI
- c) Examine the effect of pixel binning on correct identification of the ECROI

The selection of the pixel binning factor involves tradeoffs between readout speed and information loss. We evaluated binning factors of 8 (to form  $320\mu \times 320\mu$  super-pixels) and 16 (giving  $640\mu \times 640\mu$  super-pixels) using images of the test phantom acquired at low exposures. Three-dimensional pixel-value surface plots were compared to similarly



binned plots made using full exposures (Figures 1-4). The location of areas having low ADU values was the same in the low- and high-exposure plots, indicating that these binning factors did not result in unacceptable image smoothing. We then examined ROIs of 800 x 800 pixels (3200 $\mu$  X 3200 $\mu$  pixels) (Figures 5-7) and 1600 x 1600 pixels (64,000 $\mu$  X 64,000 $\mu$  super-pixels). For the 3200 $\mu$  X 3200 $\mu$  pixel ROI, a 6 x 8 grid of ROIs was established. In our experiments (Figures 5 & 6), the ROI positions were held fixed while their side lengths varied between minimum values of approximately 1.7% of the short dimension of the image, to their maximum value, equal to the center-to-center ROI spacing. Average pixel value in the 48 ROIs (Figure 5) were plotted as a function of ROI side length, in units of binned pixels (Figure 6). We then performed similar experiments for 64K  $\mu$  X 64K  $\mu$  ROIs. These data were then utilized for task 2 experiments (below) to calculate the contribution of signal to the total variance of the ECROIs.

## **Task 2. Identify the contribution of signal to the total variance in the ECROI.**

This entails distinguishing between contributions to the variance within the ECROI from breast structure and from noise (e.g., x-ray quantum noise or  $\sigma_{\text{quantum}}$ , and additive/system noise or  $\sigma_e$ ) in the pre-exposure images. We have used two pre-exposures to permit pixel fluctuations arising from the signal relating to breast structure to be distinguished from those arising from noise. The ECROI is determined from the first pre-exposure. Only detector modules containing the ECROI are read out on the second pre-exposure. Pre-exposure times and initial kVp are scaled according to compressed breast thickness ( $\geq 6.5$  cm:30 kVp; 6 cm:29 kVp; 5.5 cm:28 kVp; 5 cm:27 kVp; 4.5 cm:26 kVp;  $\leq 4.0$  cm:25 kVp). Initial choices for pre-exposure times and kVp are based on values calculated to result in a MGD of approximately 150 mrad to a 50% fat / 50% fibroglandular breast in an exposure time of approximately 1 sec.

Criteria for optimization of tube voltage and external filtration in digital mammography differ from those used in screen-film mammography. This is because the separation of the processes of acquisition and display in the former permits contrast of individual structures to be adjusted when the image is displayed. It is therefore possible to detect objects with low subject contrast provided that the image signal to noise ratio (SNR) is adequate. Thus, rather than maximization of contrast within the constraints of acceptable film darkening and patient dose, beam optimization in digital mammography requires maximization of the image SNR, constrained by acceptable patient dose.

To identify optimum technique factors, the following figure of merit was used:

$$\text{FOM} = (\text{SNR})^2 / \text{MGD},$$

Where MGD is mean dose to the glandular portion of the breast, and the SNR is Rose's suggested minimum value of 5 [1].

Using simple phantoms with known signals (disks, holes, etc.) that result in signal-induced variances that are easily determined, we calculated the ECROI SNR. Breast tissue equivalent material corresponding to 3 different fat/glandular ratios was used to simulate a range of breast thicknesses and densities. Look-up tables were generated with starting pre-exposure time and kVp for varying breast composition/thickness (288 test conditions) as input data. These data were further refined in task 3 experiments using



anthropomorphic breast phantoms that more closely approximate the spectral content of human breast tissue (see below).

**Task 3. Determine how breast structure relates to measured variances.** We selected a broad range of breast thickness and radiodensity from our Digital mammography patient image database to empirically determine the contribution to the total variance that arises from breast structure (signal). In order to obtain the best possible estimate of the variance associated with normal breast parenchyma, we selected ROIs from sub-areas of mammograms with obviously high SNR. In those ROIs, the average pixel value and system gain was used to calculate the x-ray quantum variance,  $\sigma_{\text{quantum}}^2$ . Using the measured system noise,  $\sigma_e$ , the contribution to the total variance,  $\sigma_{\text{total}}^2$ , from breast tissue was calculated from:

$$\sigma_{\text{signal}}^2 = \sigma_{\text{total}}^2 - \sigma_{\text{quantum}}^2 - \sigma_e^2$$

After the 2 pre-pulses, we calculated  $\sigma_{\text{noise}}^2$  and  $\sigma_{\text{signal}}^2$  and used the empirically determined relationship between  $\sigma_{\text{signal}}^2$  and  $I_{\text{max}} - I_{\text{min}}$  to infer the magnitude of the signal. The ratio of the inferred signal to  $\sigma_{\text{noise}}$  is the SNR following the pre-exposure. This was then used to select exposure parameters for the full exposure. If only the exposure *time* is to be selected (phototiming mode), this is straightforward since  $I_{\text{max}} - I_{\text{min}}$  is directly proportional to mAs and since the quantum noise,  $\sigma_q$ , increases as the square root of the exposure time. In the CCD-based TREX system, the system noise ( $\sigma_e$ ) increases as the square root of the exposure time because of the accumulation of thermal electrons in the CCD pixels. This noise was previously characterized over a large range of exposure times.

### **Results of Phantom Experiments Performed for Tasks 2 & 3:**

Following are example plots of measured signal, SNR, and the FOM, as a function of kVp, for a 70/30 fibroglandular/fat equivalent phantom composition, using the signal from the microcalcification-equivalent material. These data were obtained from the DM system at Johns Hopkins. The results of these studies were presented at the 5<sup>th</sup> International Workshop on Digital Mammography, Toronto, CA, June 11-14, 2000.

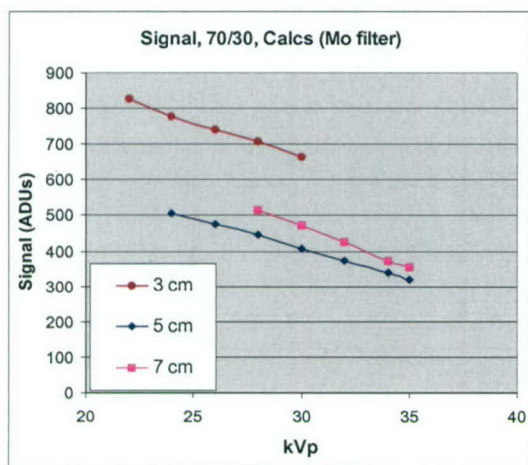


Figure 1

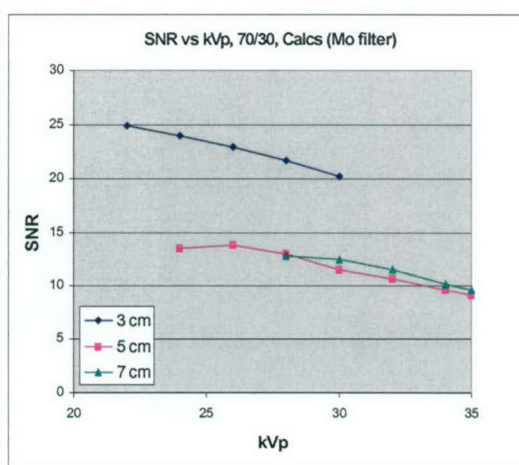


Figure 2

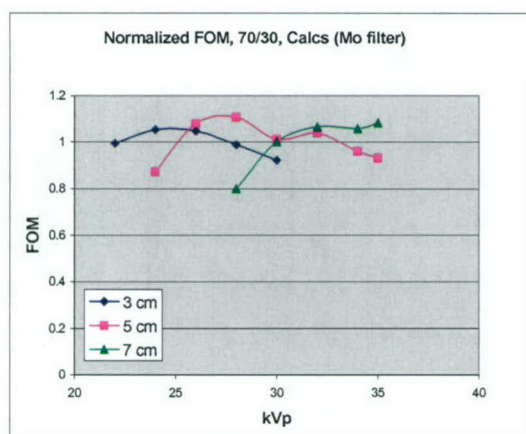


Figure 3

Nine different phantoms were assembled to simulate breasts of three different thicknesses (3 cm, 5 cm, and 7 cm), and three different attenuation equivalent adipose/fibroglandular mass ratios (30/70, 50/50, and 70/30). All blocks of a given phantom had the same adipose /fibroglandular ratio, except for two 5 mm thick blocks, common to all phantoms, that are 100% adipose equivalent. These blocks were placed at the top and bottom of the stack to simulate skin (see figure 4). In each phantom stack assembled, the centrally located block in the stack (the signal block) contained a series of test objects. For the data reported here, the test objects of interest were two stepwedges, one each of calcification equivalent and mass equivalent material. The mass equivalent stepwedge has the same x-ray attenuation as 100% glandular equivalent material, and the microcalcification equivalent step wedge is composed of calcium carbonate. Figure 5 is a schematic of a signal block showing the dimensions of the block and step wedges (other test objects present in the signal block have been omitted for clarity). The thickness of all signal blocks is 2 cm. Images were obtained in manual mode with the phantoms positioned at



the chest wall edge of the receptor, centered left to right. Exposure time was selected to give approximately the same average pixel value in the phantom background area for each phantom/technique combination. For each combination two images were obtained with identical exposure times for the purpose of image subtraction, taking care not to move the phantom between the two exposures. At each site, entrance exposures (mR/mAs) and half value layers (HVLs) were measured for each target/filter/kVp combination used.

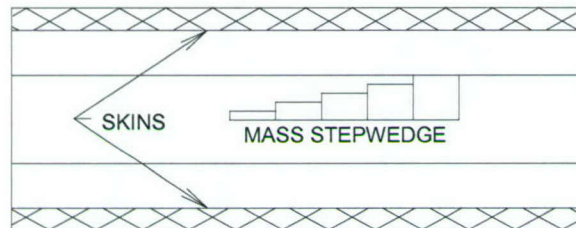


Figure 4: Side view of a 5 cm thick phantom, comprised of one 2 cm thick signal block, two 1 cm thick blank blocks, and two 0.5 cm thick skins.

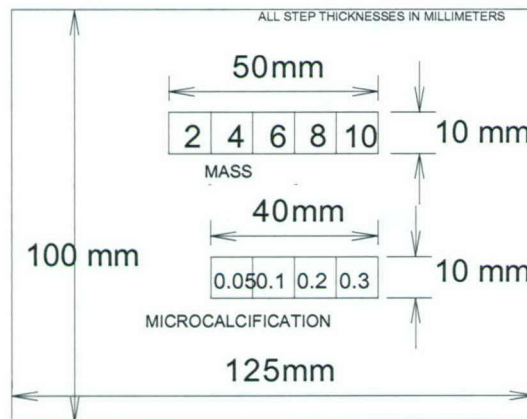


Figure 5: Schematic diagram of a signal block

### ECROI Analysis:

Signal was defined as the difference between the average pixel values in a region of interest (ROI) centered on an individual step (but not including the step boundaries), and an equal sized ROI located immediately adjacent to the step, but containing only background. To quantify the image noise, the two images of a given phantom, obtained at a common technique, were subtracted. Image subtraction was performed to remove fixed pattern noise associated with phantom defects, detector non-uniformity, and the heel effect. Noise in a single image was defined as the rms pixel-to-pixel fluctuations in an ROI of 1109 x 511 pixels in the difference image, divided by the square root of two.

### Evaluation of acceptable mean glandular dose:

The MGD for each phantom was calculated using its known thickness and composition, and the measured HVL and mR/mAs values from each DM system. For Mo/Mo and Mo/Rh spectra, the parameterized dose tables of Sobol and Wu were utilized to obtain the glandular dose per unit exposure [2]. For the W/Al spectra, normalized (to entrance exposure) MGD values were obtained from the data of Stanton et al. [3]. Their data were extrapolated to 3 cm breast thickness, and interpolation between their published HVL curves was used to obtain correction factors for the particular glandular volume fractions (0.22, 0.40, and 0.61, corresponding to glandular mass fractions of 0.30, 0.50, and 0.70, respectively) used in our study. For the W/Rh spectra, the calculations of Boone were utilized, interpolating between his published HVL and adipose/fibroglandular composition values [4]. All FOM values were obtained by dividing the square of the SNR by the MGD, expressed in units of  $10^{-5}$  Gy (1 mrad).

The measured HVL values for the seven specific target/filter combinations tested at the three sites, as a function of kVp, are shown in Figure 3. Figure 4 shows the corresponding normalized MGD,  $D_{gN}$ , calculated for each of the seven spectra, plotted versus the measured HVL. Similarly, Figure 8 shows  $D_{gN}$  for each target/filter combination tested, plotted versus kVp. The general tradeoff between loss of contrast and reduction in MGD with increasing kVp is illustrated in Figure 9. In this example, the measured contrast of the 0.3 mm thick (thickest) calcification step in shown for the 5 cm thick, 50/50 phantom.

SNR versus kVp, and the corresponding FOM values vs. kVp have been determined. Figures 10 and 11 show the results obtained for the 300 micron thick step of the calcification stepwedge in the three 50/50 composition phantoms. To illustrate the applicability of these data to objects, the dependence of the FOM on the step thickness for both types of stepwedges is presented in Figures 12 and 13. These data are from images obtained using a Mo/Mo target/filter combination to image a 5 cm thick, 50/50 composition phantom. Finally, Figures 14-16 illustrate the effect on the FOM of changing breast composition, holding breast thickness fixed. Signals were calculated using the 10 mm thick mass equivalent step.

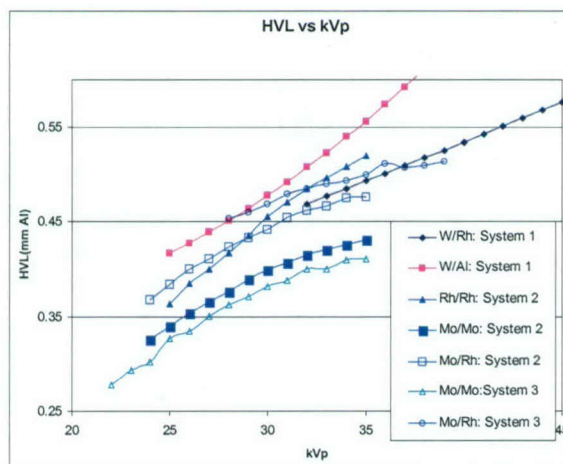


Figure 6: Measured HVLs , plotted versus



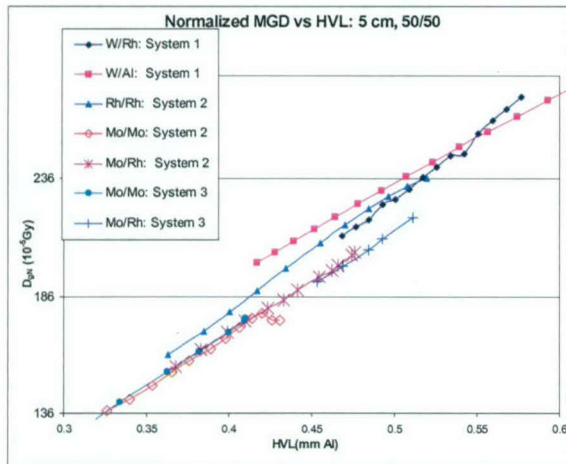


Figure 7: Normalized mean glandular dose versus HVL, assuming a 5 cm thick, 50/50 phantom

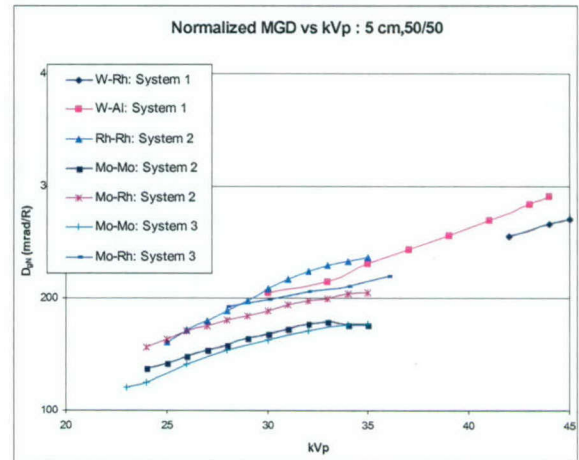


Figure 8: Normalized mean glandular dose vs. kVp assuming a 5 cm thick, 50/50 phantom

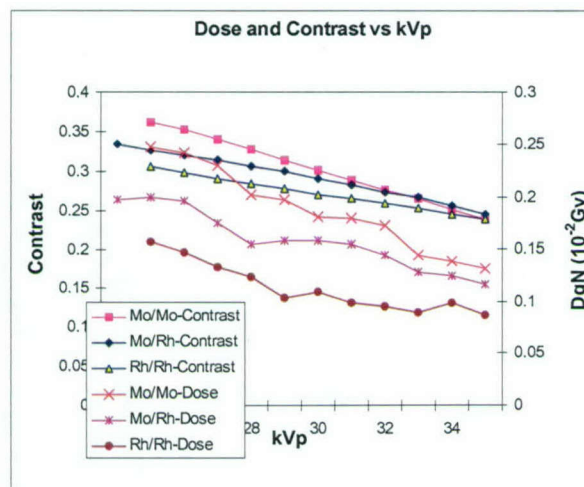


Figure 9: Dose and contrast versus kVp using the 0.3 mm calcification step in a 5 cm thick, 50/50 phantom



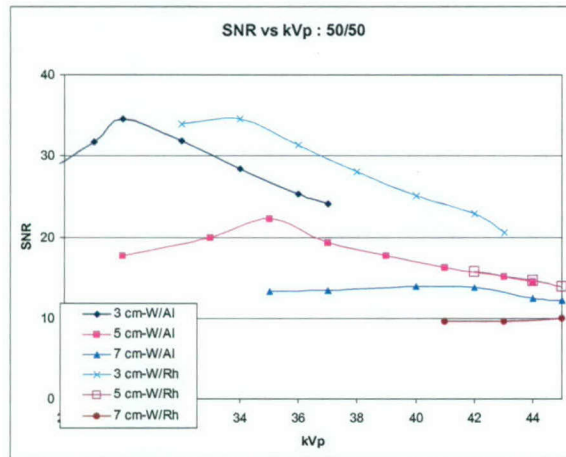


Figure 10: SNR vs. kVp.

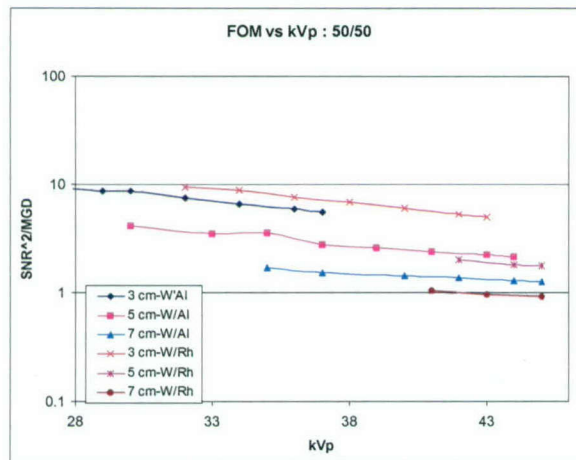


Figure 11: FOM vs. kVp.

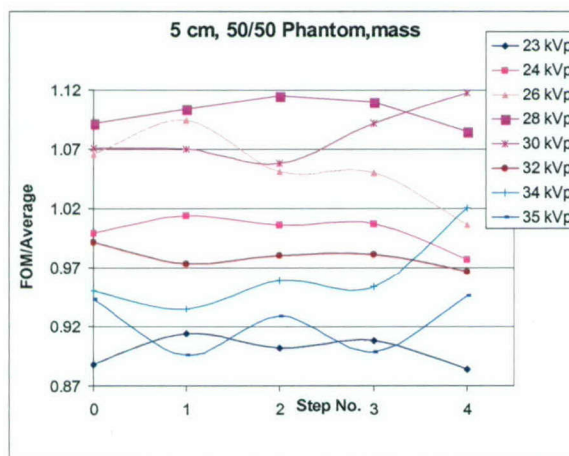


Figure 12: FOM values for the five steps of the mass stepwedge, normalized by the average value for each step. The average FOM values ranged from 0.2 (step 0) to 0.011 (step 4). Imaging data from the 5 cm 50/50 phantom.

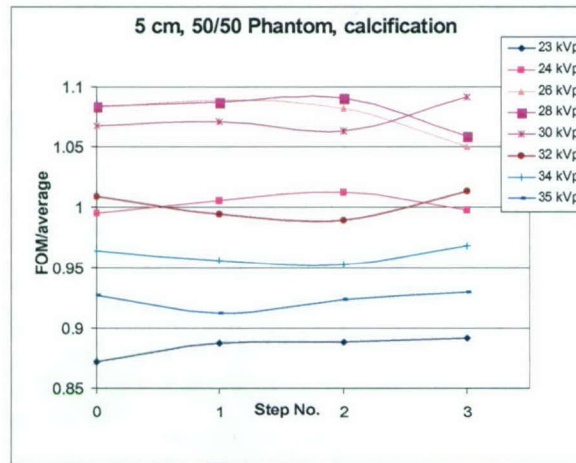


Figure 13: FOM values for the four steps of the calcification stepwedge, normalized by the average value for each step. The average FOM values ranged from 1.4 (step 0) to 0.64 (step 3). Data are imaging the 5 cm 50/50 phantom.

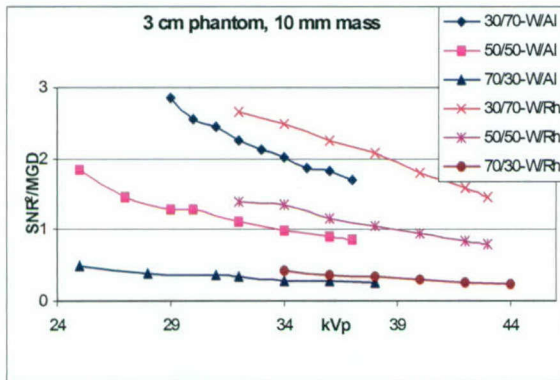


Figure 14: FOM vs kVp for 3 cm thick phantoms of three compositions.

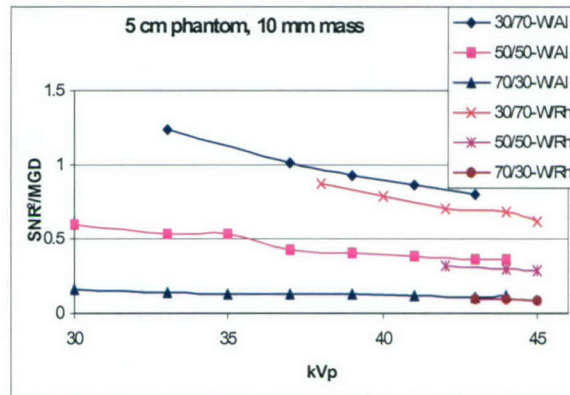


Figure 15: FOM vs kVp for 5 cm thick phantoms of three compositions

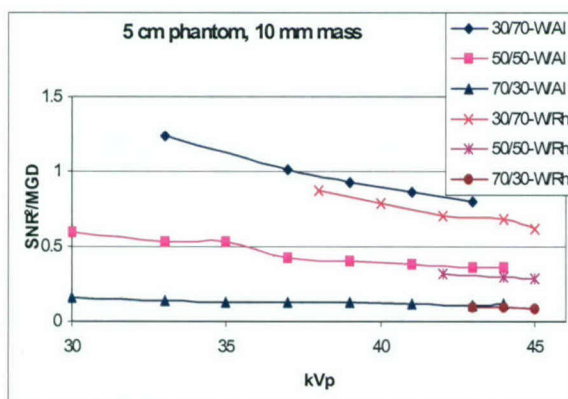


Figure 16: FOM vs kVp for 7 cm thick phantoms of three compositions.

#### Task 4. Optimize mAs, kVp, and Filter Selection Based on the Results of the Pre-exposures.

Optimization is based on maximization of the figure of merit:  $FOM = (SNR^2 / MGD)$ . We have used the added information provided by the spatially varying signal levels in the pre-exposure ROIs to calculate a more refined estimate of the MGD than is possible using simply compressed thickness. To do this, the mean pixel value in each ROI is used to determine the relative transmission through the breast at that location. In regions of uniform thickness (all regions whose entrance surface is in direct contact with the compression paddle), variations in x-ray transmission are due to variations in breast composition. The region of the breast above each ROI is assumed to consist of two skin and subcutaneous layers with a uniform mixture of adipose and fibro-glandular tissue in between. The x-ray transmission through each region determines an adipose/fibro-glandular composition ratio. Thus, for a given kVp, filter, and mAs, the MGD for the region of the breast above each ROI can be calculated separately, and the result summed to obtain an average MGD.

#### Preliminary Results: Task 4:

Software has been developed for analysis of digitally acquired mammograms. The primary two questions to be addressed by these analysis tools may be generalized as follows:

- 1) Which area of the digitally obtained mammogram contains the area of greatest radiographic attenuation (the ECROI)?
- 2) What portion of the pixel variance in the ECROI is a result of differential breast attenuation (signal) as opposed to random fluctuations (noise)?

With respect to question 1), the immediate objectives of these programs are:

- 1) Evaluate the correlation between the number of regions of interest (ROIs) sampled and the correct identification of the ROI containing the area of greatest radiographic attenuation (the ECROI)
- 2) Evaluate the correlation between ROI size and correct identification of the ECROI



3) Examine the effect of pixel binning on correct identification of the ECROI

Figure 17 below shows an example of a digitally obtained mammogram in which a 6 x 8 grid of ROIs has been established. The figure shows the mammogram, labeled with numbers whose locations correspond to the centers of the ROIs.

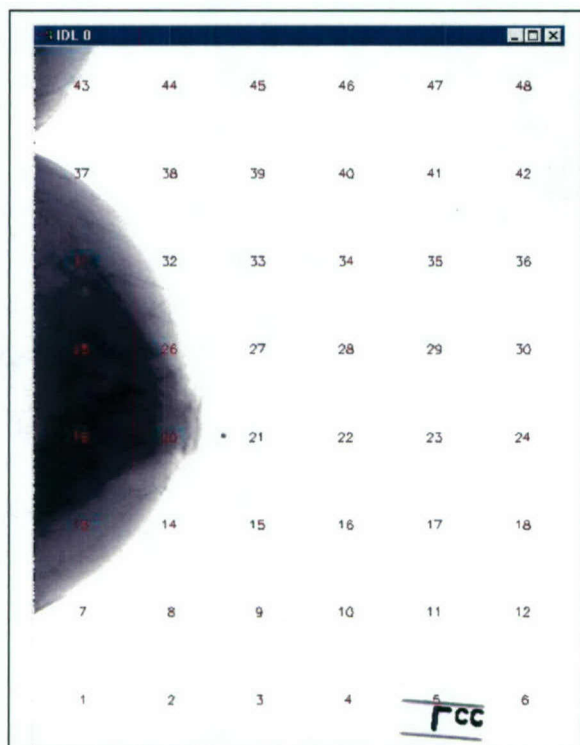


Figure 17: A digitally acquired mammogram, annotated with the locations of a 6 x 8 square grid of ROIs. The numerals are located at the centers of the square ROIs. The ROI positions are held fixed, while their side lengths are varied between minimum values of approximately 1.7% of the short dimension of the image, to their maximum value, equal to the center-to-center ROI spacing.

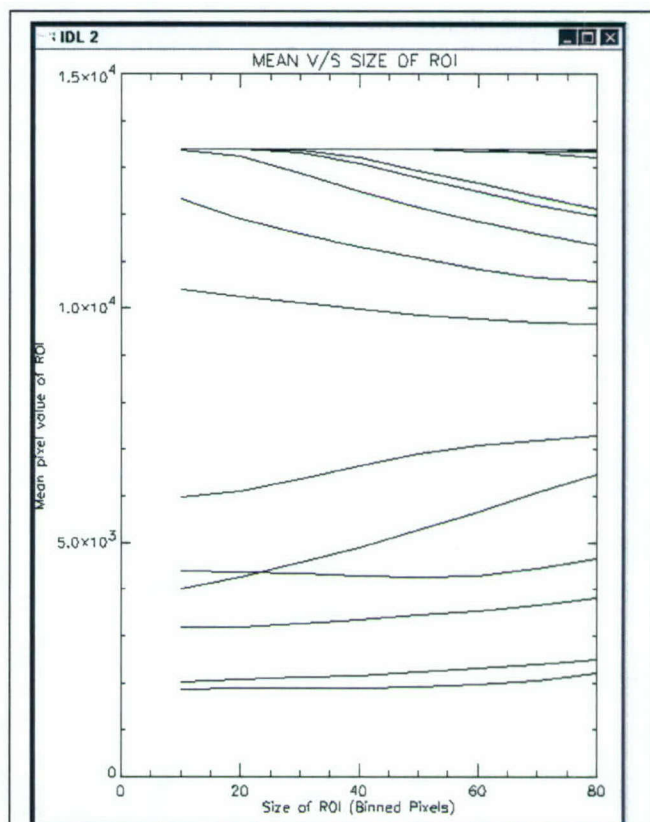
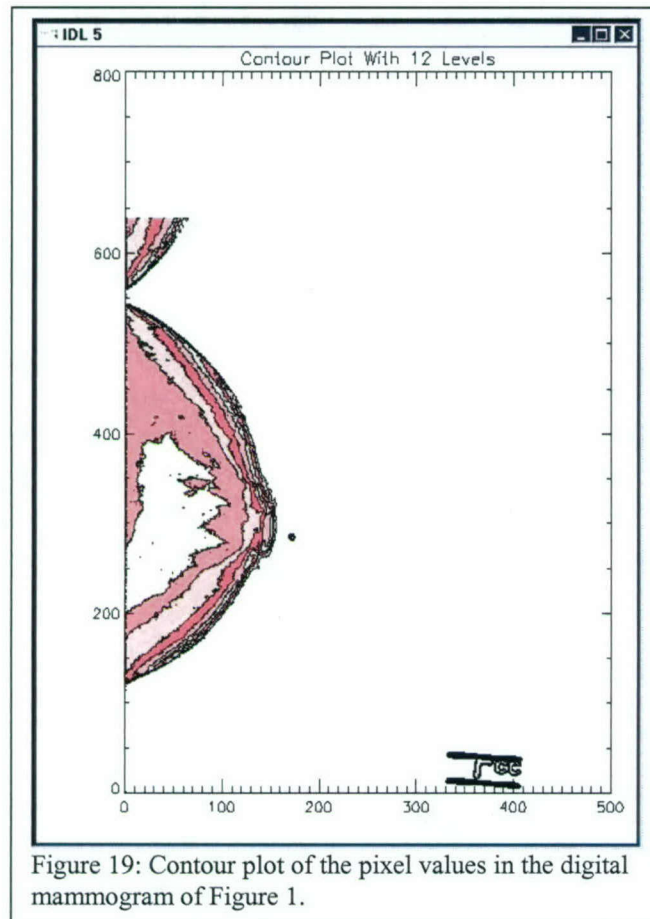


Figure 18: Average pixel value in the 48 ROIs of Figure 1, plotted as a function of ROI side length, in units of binned pixels. For the example shown, the ECROI (that with the lowest average pixel value) is the same for all ROI sizes tested. Its center is at the position labeled '19' in Figure 17. ROIs whose average pixel value is always large and constant (top of the graph) are located outside the region of the breast.

Figure 18 is a plot of the mean values of each ROI, plotted as a function of ROI size. The ROI with the lowest value is the ECROI. For the example shown, the ECROI is ROI #19. The contour plot of the pixel values, shown below in Figure 19, verifies that this is in fact the most highly attenuating portion of the breast.



We have developed analysis tools to evaluate the effect of radiographic heterogeneity on the selection of the ECROI and have performed analysis of digital mammograms of patients with a variety of compositions and breast sizes. Table 1 below provides the calculated ratios of root mean square signal to root mean noise for 20 digital mammographic images evaluated in 5 patients with a variety of breast compositions (radiodensity). For each study, the compressed breast thickness was 4 -5 cm and a 28 kVp Mo/Mo beam was used. The third column gives the total variance in the ECROI. The fifth column gives the portion of the variance that is due to noise, as determined by uniform irradiation studies. The last column gives the ratio of the RMS signal to the RMS noise. These ratios suggest the approximate magnitude of the target SNR values to be used in the AEC algorithm.

**TABLE 1: Ratio of RMS Signal to RMS Noise**

	Average	Total Variance	mAs	Noise Variance	Signal Variance	SNR
Patient 1	1422	17986	43	745	17242	4.8
	1420	11556	43	744	10812	3.8
	1504	29009	46	780	28229	6.0
	1630	23148	50	835	22313	5.2
Patient 2	2031	36416	62	1019	35397	5.9
	1964	16243	60	987	15255	3.9
	1964	25290	60	987	24303	5.0
	1972	26219	60	991	25228	5.0
Patient 3	1535	9923	47	794	9129	3.4
	1430	16615	44	748	15867	4.6
	1458	14053	44	760	13293	4.2
	1461	19624	45	762	18863	5.0
Patient 4	1577	25117	48	812	24305	5.5
	1502	20446	46	779	19667	5.0
	1547	22630	47	799	21831	5.2
	1311	35793	40	698	35095	7.1
Patient 5	2204	49051	67	1102	47949	6.6
	1727	20817	53	879	19938	4.8
	2041	22180	62	1024	21156	4.5
	2329	39980	71	1163	38816	5.8



Table 2. Log mAs versus Average ADU, Variance and Log (Sigma)

mAs	Bright 1				Bright 2				Dark 1				Dark 2			
	Average ADU	Variance	log(sigma)	log(sigma)	Average ADU	Variance	log(sigma)	log(sigma)	Average ADU	Variance	log(sigma)	log(sigma)	Average ADU	Variance	log(sigma)	log(sigma)
3	0.5	75	167	1.1	1.1	76	195	1.1	1.1	7.7	52	7.0	40	7.0	40	7.0
6	0.8	175	215	1.2	1.2	176	215	1.2	1.2	7.0	41	7.1	42	7.1	42	7.1
10	1.0	311	279	1.2	1.2	310	280	1.2	1.2	6.9	39	6.9	40	6.9	40	6.9
20	1.3	644	448	1.3	1.3	644	448	1.3	1.3	6.8	40	6.8	39	6.8	39	6.8
40	1.6	1311	803	1.5	1.5	1310	808	1.5	1.5	7.0	41	7.2	44	7.2	44	7.2
80	1.9	2637	1507	1.6	1.6	2636	1504	1.6	1.6	7.1	44	7.1	46	7.1	46	7.1
160	2.2	5306	2979	1.7	1.7	5306	2980	1.7	1.7	7.4	58	7.1	53	7.1	53	7.1
240	2.4	7984	4734	1.8	1.8	7981	4742	1.8	1.8	7.6	72	7.5	71	7.5	71	7.5
325	2.5	10832	8617	2.0	2.0	10852	7597	1.9	1.9	7.9	94	8.0	94	8.0	94	8.0
400	2.6	13376	11067	2.0	2.0	13377	11054	2.0	2.0	8.3	118	8.0	115	8.0	115	8.0

Figure 20a. Average ADU vs. mAs  
Linearity as a Function of X-ray  
Exposure

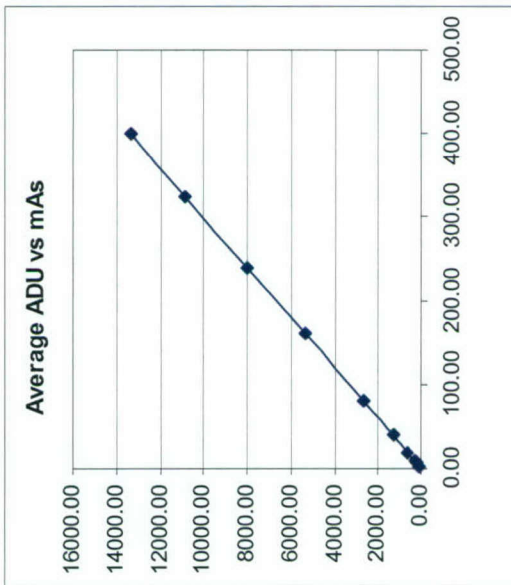


Figure 20b. log(sigma) vs log(mAs)  
Log of the SD vs. log of the mAs

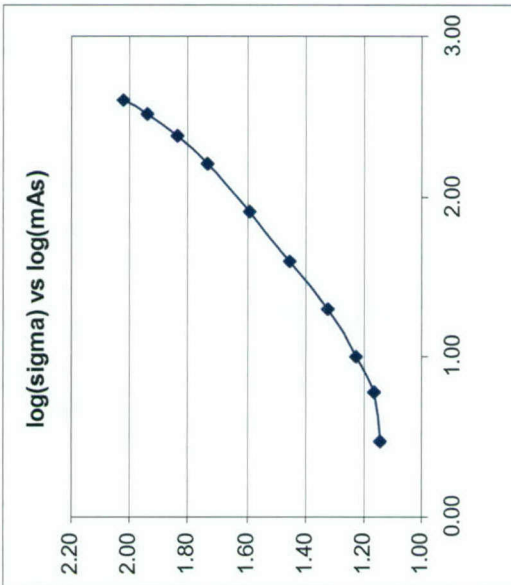
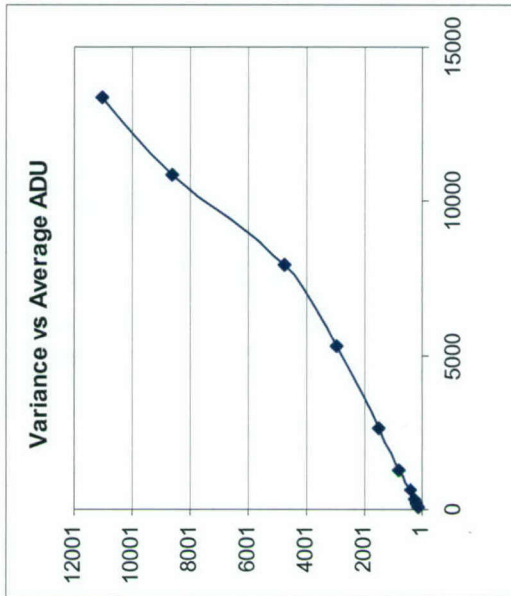


Figure 20c. Variance vs. Average ADU

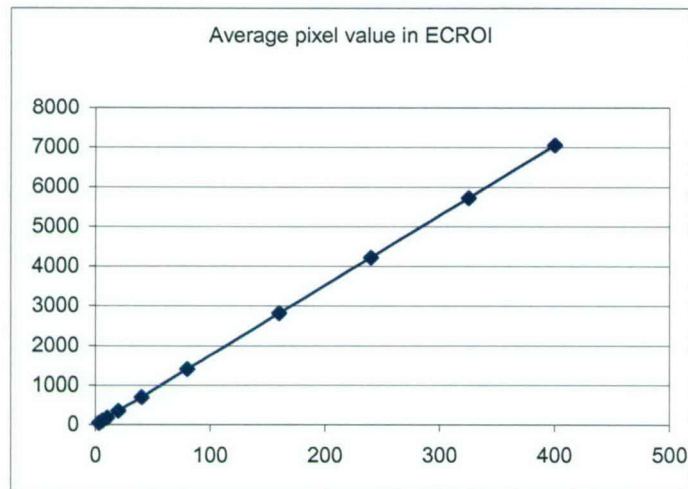


We have carefully evaluated linearity as a function of x-ray exposure (Table 2 & Figure 20a) with phantom experiments using a 4cm acrylic phantom imaged at 28 kVp. The quantum limited range of operation was determined from a log-log plot of the pixel variance vs the mAs (Figure 20b). As is shown, the linear region between  $\sim 1.0$  and  $2.5$  on the horizontal axis (Figure 20b) indicated quantum limited operation. Below  $\log(\text{mAs}) = 1.0$ , the system noise constitutes a significant part of the total noise, and above  $\log(\text{mAs}) = 2.5$ , there is a slight departure from quantum limited operation, probably due to imperfectly corrected fixed pattern noise at these high exposure levels. This departure can also be seen in the two data points in the upper right portion of Figure 20c. We will use the quantum limited region in our calculation of the final mAs, based on the measured signal variance (pixel variance due to differential breast attenuation) in the ECROI following pre-exposure. .

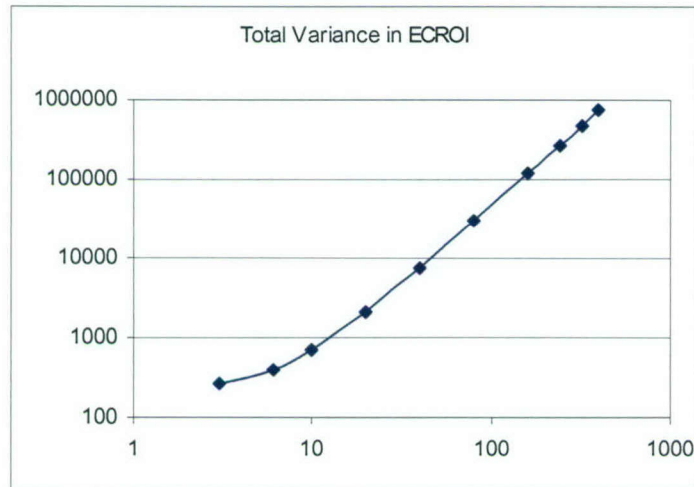
We have also developed analysis programs for determination of the pixel variance due to differential breast attenuation (signal variance), and are characterizing intrinsic detector noise. Table 3 below provides data on the total variance in the ECROI, including its components due to signal and noise.

Table 3. Total Variance in the ECROI as a function of the Signal and Noise Components					
mAs	Average	Total Variance	Noise Variance	Signal Var	sqrt(sig var)
3	43	262	167	95	10
6	94	409	215	194	14
10	166	700	279	421	21
20	343	2110	448	1662	41
40	698	7548	803	6745	82
80	1401	29174	1507	27667	166
160	2813	116440	2979	113461	337
240	4224	261613	4734	256879	507
325	5724	481110	8617	472493	687
400	7056	732557	11067	721490	849

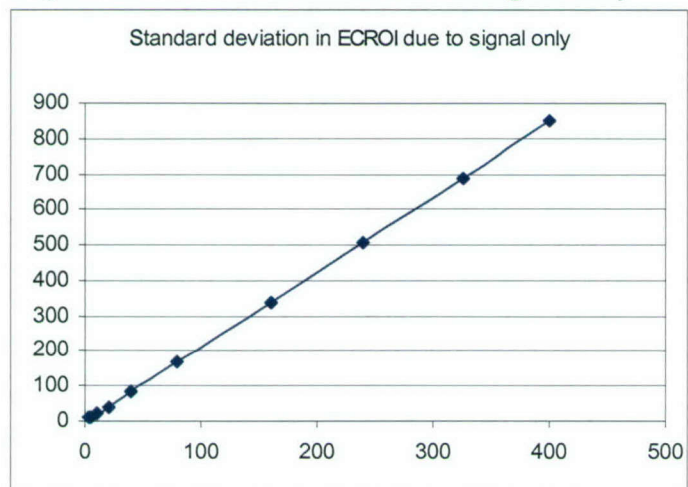
**FIGURE 21a. Average Pixel Value in ECROI**



**Figure 21b. Total Variance in ECROI**



**Figure 21c. S.D. in ECROI due to Signal only**





These results demonstrate that the total variance in the ECROI is the arithmetic sum of the signal and noise variances. As shown in Figure 21c, the signal variance is proportional to the square of the mAs, as would be expected for a linear system. Therefore, determination of the total variance at any given mAs, along with the known noise variance at that mAs, permits calculation of the SNR for all mAs values. In the context of AEC development, this means that we can quickly assess the RMS signal variance in the ECROI following pre-exposure at low mAs, and extrapolate to the target mAs value that will result in the desired SNR.

### ***Key Research Accomplishments: Progress Since Last Report***

Over the last 12 months, we evaluated radiation exposures and image quality in a population of women (n=245) undergoing both conventional film mammography (FM) and DM. Four images or "views" were performed by each modality. Information regarding the patients' age, breast tissue radiodensity, the breast thickness when compressed for the mammograms, and exposure factors were collected. The radiodensity of breast tissue on a mammogram correlates with the ease or difficulty of reading the study; cancers are more easily detected in tissue composed entirely of adipose tissue (not radiodense) than in breast tissue that is more radiodense (i.e., comprising fibroglandular rather than adipose tissue).

For each modality, we calculated the mean glandular radiation (MGD) dose for each of the 4 images comprising each subject's DM and FM and performed an assessment of image quality using radiologists certified in mammography. Here, the traditional FMs using a standard radiographic "light box" and DMs were evaluated on a soft copy workstation equipped with high resolution CRT monitors for displaying the digital images and with the capability to adjust the image brightness, contrast, and window levels for optimal interpretation. For each modality, the radiologist readers completed an evaluation form, providing subjective assessments of image quality with respect to visualization of critical breast anatomic structures, using a rating scale of 1=poor to 5=excellent quality.

### **Results**

The MGD for each of 4 breast images associated with each case (245 DMs and 245 FMs, therefore 980 DM and 980 FM images) was calculated and evaluated by analysis of variance with repeated measures for modality and view (Table4). The average MGD per image was greater for FM than for DM: 217.1mrad vs. 208.0 mrad ( $p = 0.0300$ ;  $F(1,244) = 4.76$ ). The magnitude of the MGD difference varied with the particular mammographic view.

<b>Table 4. MGD (mrads) per Mammographic View</b>				
<b>Modality</b>	<b>Lt MLO</b>	<b>Rt MLO</b>	<b>Lt CC</b>	<b>Rt CC</b>
FM	224.8	227.1	207.6	209.1
DM	212.8	212.2	205.1	201.9
$p = 0.0214$ ; $F(3,732) = 3.54$				
MGD=mean glandular dose, mrad=millirads, Lt=left, Rt=right, MLO=mediolateral oblique view, CC=craniocaudal view, FM=film mammography, DM=digital mammography				

The overall MGD (adding together the dose from all four views) for FM and DM was studied by analysis of variance with a grouping factor for breast radiodensity using FM as the gold standard and a repeated measure for mammographic modality. Overall MGD was higher for FM than for DM: 924.5 mrad vs 855.2 mrad ( $p = 0.0096$ ;  $F(1,241) = 6.81$ ). The difference in overall dose between film and digital DID NOT depend on breast radiodensity ( $F(3,241) = 1.53$ ,  $p = 0.2064$ ).

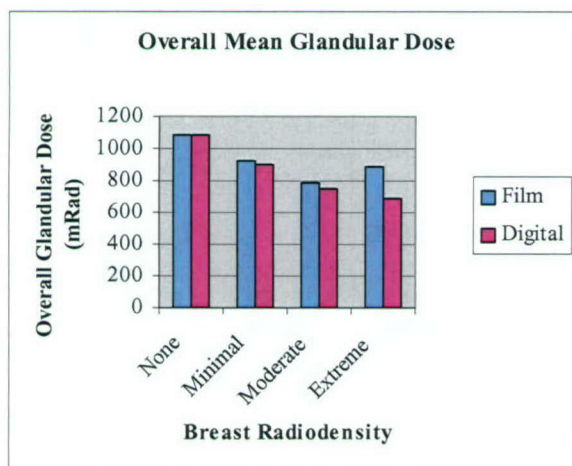


Figure 22

Table 5. Mean Image Quality for FM and DM by Breast Density		
Breast Radiodensity	FM	DM
Not radiodense	3.9	4.7
Minimally radiodense	3.8	4.7
Moderately radiodense	3.7	4.7
Extremely radiodense	3.0	4.4
$p = 0.1516$ ; $F(3,209) = 1.78$		

The image quality ratings (1=poor to 5=excellent) were lower for FM than for DM: 3.6 vs 4.6 ( $p < 0.0001$ ;  $F(1,209) = 185.96$ ). The magnitude of the quality advantage for DM depended on the specific features being evaluated with the skin line on DM being better visualized than on FM ( $p < 0.0001$ ,  $F(3,627) = 49.72$ ) (Table 6). However, the advantage for DM did not depend on breast radiodensity (Figure 23).



**Table 6. Mean Quality Rating for FM and DM of Specific Image Features**

	Posterior Tissue	Retroareolar tissue	Retroareolar Structures	Skin Line
Film	3.6	3.7	3.8	3.2
Digital	4.6	4.6	4.6	4.8

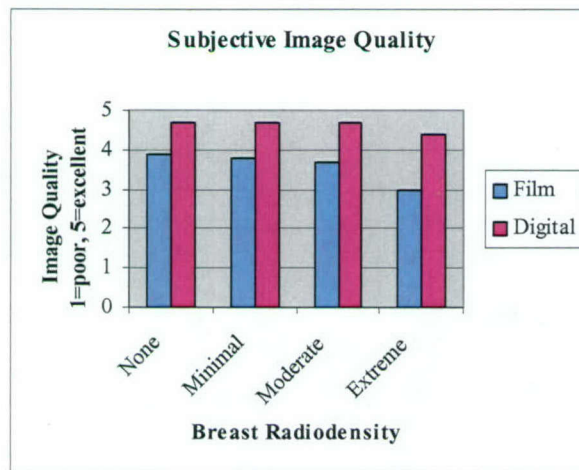


Figure 23



## Reportable Outcomes:

### Abstracts & Presentations:

The 1999 Radiological Society of North America, Chicago, IL, November 27- December 3, 1999: "Development of a quality control system for full-field digital mammography". MJ Yaffe, MB Williams, LT Niklason, GE Mawdsley, AD Maidment, Radiology 209(P) (1999) 160.

The 5<sup>th</sup> International Workshop on Digital Mammography, Toronto, CA, June 11-14, 2000: "Beam Optimization for Digital Mammography". MB Williams, M More, V Venkatakrishnan, L Niklason, MJ Yaffe, G Mawdsley, A Bloomquist, A Maidment, D Chakraborty, C Kimme-Smith, LL Fajardo.

Submitted: 2004 RSNA", November 2004. "Breast Radiation Dose for Conventional Film Versus Digital Mammography", Grignon L, Berbaum K, Williams MB, More MG, Maxwell S, McGruder A, Fajardo L. (Included in appendix).

### Publications:

Jung W, Liu H, **Fajardo LL**. Contrast detail detectability of a full field digital mammography system. SPIE Proceedings 1999;3595:186-192.

Liu H, Jiang H, Chen W, **Fajardo LL**. Lens distortion in optically coupled digital x-ray imaging. Medical Physics 2000;27(5):906-912.

Williams MB, Mangiafico PA, Simoni PU. Noise power spectra of images from digital mammography detectors. Med Phys 2000;6(7):1279-1293.

### Conclusions:

The analysis of SNR and FOM as a function of kVp, shown in Figures 10 and 11, indicates that although the image SNR tends to decrease monotonically for all systems with increasing kVp, the accompanying MGD reduction results in fairly flat FOM curves. This is primarily due to tube loading, since it was not possible to obtain the same exit exposure at all kVps (that is, the tube output was insufficient to compensate for the lower transmission through the phantoms). Thus the falling SNR (and the falling MGD) with decreasing kVp are really consequences of falling exposure.

For a given phantom/technique combination, the SNR, and thus the *magnitude* of the FOM, increases with increasing step thickness for both types of stepwedge. However, the *shape* of the FOM vs. kVp curves for a given target/filter/phantom combination are essentially independent of step thickness, and are similar for mass and calcification equivalent signals. This is illustrated by the example shown in Figures 12 and 13. This implies that the result of the optimization is not sensitively dependent on signal amplitude.



Figures 14-16 illustrate a clear advantage to using rhodium filtration for thin breasts, but that for breasts 5 cm or thicker, aluminum filtration becomes increasingly advantageous. Similar statements can be made for the molybdenum target systems tested, where molybdenum filtration was superior for 3 cm phantoms of all compositions, but rhodium filtration produced better results for 5 and 7 cm thick phantoms of all compositions. These data suggest that the choice of external filtration is potentially more significant in determination of the overall FOM of a DM system than is choice of tube voltage.

Fahrig and Yaffe developed a model for optimizing spectral shape in digital mammography, and used it to calculate kVp values producing maximum SNR at a fixed dose for W and Mo spectra [5]. They found that, for a fixed MGD of 0.6 mGy (60 mrad), the peak SNR occurred in the 24-31 kVp range (W spectrum) and 25-29 kVp range (Mo spectrum) for 4 – 8 cm breast thickness, and 50/50 breast composition. Their results were the same, whether the lesion type modeled was infiltrating ductal carcinoma or microcalcification.

Jennings et al. used a computational approach to identify maximum FOM values ( $FOM = SNR^2/MGD$ ) for a variety of target/filter combinations, and breast thicknesses [6]. They found that for a Mo/Mo beam used to image 3-6 cm, 50/50 breasts, the FOM peaks at 27-28 kVp, and changes slowly with changing kVp near the peak values. Very similar FOM vs. kVp curves were obtained for Mo/Mo, Mo/Rh, and W/Al spectra, applied to 6 cm thick, 50/50 composition breasts. The general trends in our data appear to be consistent with those of these previous studies.

Our results using the Lorad CCD-based detector demonstrate that the total variance in the ECROI is the arithmetic sum of the signal and noise variances, and that knowledge of detector noise characteristics for a given attenuating thickness and kVp, permits the RMS variance due to differential breast attenuation to be obtained. Because the system is linear with respect to x-ray fluence, the signal variance is proportional to the square of the mAs. Therefore, calculation of both the signal and noise variance at any given mAs is possible, enabling permitting calculation of the SNR as a function of mAs.

Implementation of the first generation of automatic exposure control device on the digital mammography system results in images having satisfactory image quality, SNR and mean glandular dose. For 16 patients undergoing both conventional mammography and digital mammography, the implemented AEC for the digital system performed satisfactorily. We now have nearly complete data to finalize the algorithms for a functional AEC device for the experimental digital mammography system.

Our data indicate a statistically significant trend toward better image quality for DM. Although the image quality ratings are subjective, we are encouraged that quality is at least comparable and perhaps better than conventional FM. A statistically significant reduction in overall MGD and in MGD per view for DM was also measured. Thus, lower radiation exposures can be achieved with DM while maintaining subjective image quality. These results encourage further investigation into the dose reduction capabilities of DM as this new technology disseminates more widely into clinical use for breast cancer screening.

## References

1. Rose A. Vision: Human and Electronic. Plenum Press, New York, N.Y., 1973.
2. Sobol WT and Wu, X. Parameterization of mammography normalized average glandular dose tables. Medical Physics 24(4), 547-555. 1997.
3. Stanton L., Villafana, T., Day, J., and Lightfoot, D. (1984). Dosage evaluation in mammography. Radiology 150, 577-584.
4. Boone, J. (1999). Glandular breast dose for monoenergetic and high-energy x-ray beams: Monte Carlo assessment. Radiology 213, 23-37.
5. Fahrig, R. and Yaffe, M. (1994). Optimization of spectral shape in digital mammography: Dependence on anode material, breast thickness, and lesion type. Med.Phys. 21, 1473-1481.
6. Jennings, R.L., Quinn, P.W., Gagne, R.M., and Fewell, T.R. (1993). Evaluation of x-ray sources for mammography. Proc SPIE 1896, 259-268.

## Personnel Receiving Support from this Grant:

Laurie L. Fajardo, M.D.  
Mark B., Williams, Ph.D.  
Sandy Maxwell. RTRM  
Allen McGruder  
Laurent Grignon, MS

## Appendix

Publication Reprints



# Breast Radiation Dose for Conventional Film Versus Digital Mammography

Grignon L, Berbaum K, Williams MB (UVa), More MG (UVa), Maxwell S, McGruder A, Fajardo L

## Background/Rationale

Breast cancer is the most commonly diagnosed cancer in women. Early diagnosis of breast cancer by screening mammography plays a leading role in reducing the mortality and improving the prognosis of this disease.

## Limitations of Conventional film Mammography (SF)

- Reduced Image Contrast
- Limited Exposure Range
- Artifacts associated with film-based image acquisition

## Benefits of Digital Mammography (DM)

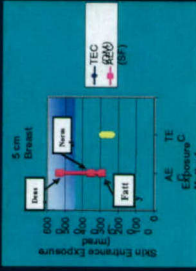
- Wider Dynamic range (improved image contrast)
- Fast and flexible image processing
- Computer Assisted Diagnosis (C.A.D.)

## Hypothesis

The use of TEC and DM provides lower radiation exposure than the traditional AEC method of conventional film mammography without degrading, and perhaps improving, image quality.

## Dose Determination in SF vs. DM

SF - For SF, the use of *Automatic Exposure Control* (AEC) devices is the standard method to set the patient image exposures. In this method, a small sensor behind the film and under the central portion of the breast determines the amount of radiation that passes through the breast to expose the film image. The AEC sensor terminates the exposure at the proper level to provide the correct optical density.



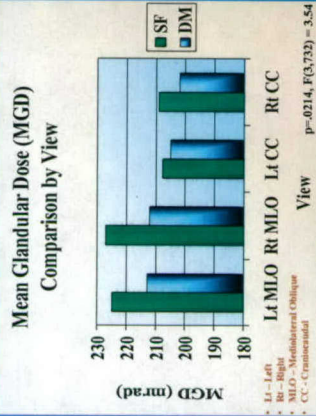
The entrance "skin" exposure for both AEC and TEC exposures obtained on SF and DM, respectively, for 5 cm thick breast phantoms having fatty, normal, and dense "tissue" compositions.

DM - In DM, exposure determination is based on the physics of x-ray absorption of the breast. Such a method uses the thickness of the compressed breast and the breast composition type (dense, fatty, normal) to compute the desired kVp (x-ray exposure) and mAs (dose) to optimally penetrate and image the breasts. This method is known as *Tissue Exposure Control* (TEC), and has the advantages of not subjecting the breast to unnecessary radiation and providing optimal exposure technique.

## Methods

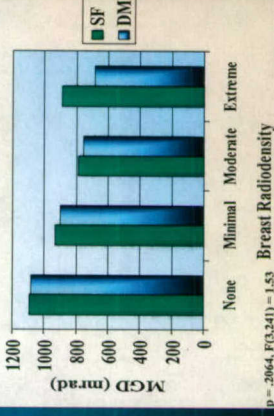
- We evaluated radiation exposures and image quality in a population of women (n=245) undergoing both conventional FM as well as DM.
- Information collected
  1. Exposure factors: mAs, kVp, filter
  2. Breast tissue radiodensity
  3. Breast compression thickness
  4. Subjective assessment of image quality by radiologists
- Calculation of mean glandular radiation dose (MGD)
- Critical breast anatomic structures were rated on scale of 1=poor to 5=excellent quality.
- Data was analyzed using paired t-tests.

## Mean Glandular Dose (MGD) Comparison



MGD was greater for SF than for DM. (217.1 vs. 208.0 mrad,  $p = 0.006$ ,  $F(1,244) = 4.76$ ). The magnitude of the difference was dependent on the view.

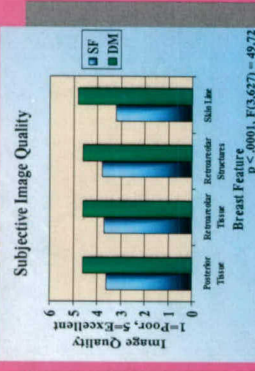
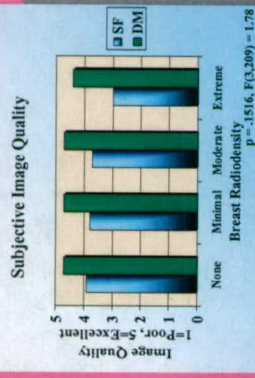
## Overall Mean Glandular Dose (MGD)



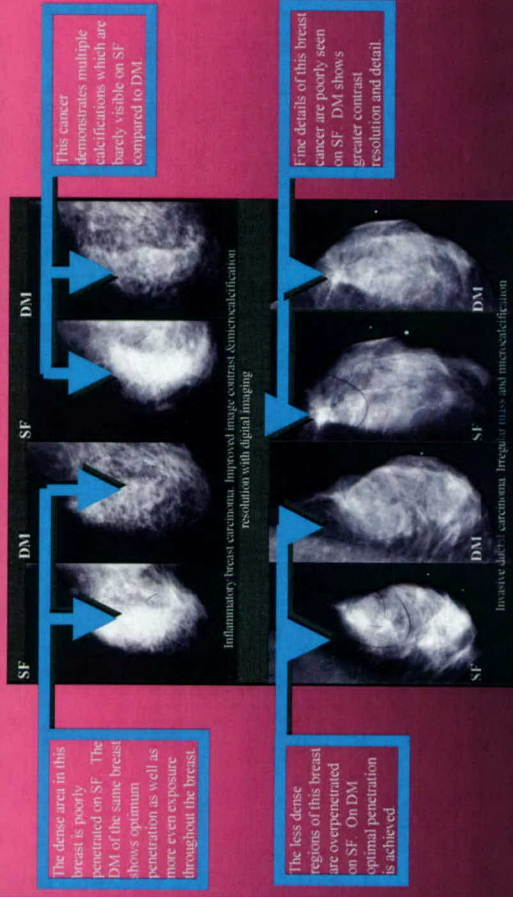
There is a trend toward higher overall MGD across breast radiodensities in SF compared to DM.

## Subjective Image Quality Comparison

For each modality (SF and DM), we performed an assessment of image quality using mammography certified radiologists. The SF mammogram was evaluated using a standard radiographic "light box." DM mammograms were evaluated on a soft copy workstation that incorporates high resolution CRT monitors for displaying the digital images and permits the radiologists to adjust the image brightness, contrast, and window levels for optimal interpretation.



The breast radiodensities in DM compared to SF.



## Conclusions

Lower radiation exposures can be achieved with DM while maintaining good subjective image quality. These results encourage further investigation into the dose reduction capabilities of DM as this new technology disseminates more widely into clinical use for breast cancer screening.

## References

1. Niklason L.T., Barnes G.T., Rubin E. Mammography: phototimer technique chart. Radiology, 1985, 157: 539-540.
2. Sobol W.T. and Wu, X. Parameterization of mammography: normalized average glandular dose tables. Medical Physics 24(4), 547-555 1997.



# Lens distortion in optically coupled digital x-ray imaging

Hong Liu,<sup>a)</sup> Hangyi Jiang, and Laurie L. Fajardo

Department of Radiology and Biomedical Engineering, Johns Hopkins University, Baltimore, Maryland 21205

Andrew Karellas

Department of Radiology, University of Massachusetts Medical Center

Wei R. Chen

Department of Physics and Engineering, University of Central Oklahoma

(Received 8 March 2000; accepted for publication 10 March 2000)

The objectives of this research are to analyze geometrical distortions introduced by relay lenses in optically coupled digital x-ray imaging systems and to introduce an algorithm to correct such distortions. *Methods:* The radial and tangential errors introduced by a relay lens in digital x-ray imaging were experimentally measured, using a lens-coupled CCD (charge coupled device) prototype. An algorithm was introduced to correct these distortions. Based on an x-ray image of a standard calibration grid, the algorithm first identified the location of the optical axis, then corrected the radial and tangential distortions using polynomial transformation technique. *Results:* Lens distortions were classified and both radial and tangential distortions introduced by lenses were corrected using polynomial transformation. For the specific lens-CCD prototype investigated, the mean positional error caused by the relay lens was reduced by the correction algorithm from about eight pixels (0.69 mm) to less than 1.8 pixels (0.15 mm). Our investigation also shows that the fourth order of polynomial for the correction algorithm provided the best correction result. *Conclusions:* Lens distortions should be considered in position-dependant, quantitative x-ray imaging and such distortions can be minimized in CCD x-ray imaging by appropriate algorithm, as demonstrated in this paper. © 2000 American Association of Physicists in Medicine. [S0094-2405(00)03705-6]

Key words: lens distortion, optically coupled x-ray imaging system, camera calibration

## I. INTRODUCTION

Both fiber optically coupled and lens-coupled CCD x-ray imaging systems have been used in digital mammography and digital radiography.<sup>1-3</sup> The cascaded imaging chain consists of a scintillator, an optical component (either a relay lens or a spatial coherent fiber bundle), and an electronic imager, such as a CCD imager.<sup>4-6</sup> Obviously, the optical properties of the lens, or the fiber, can affect the quality of the x-ray imaging significantly. In our previous communications, the characteristics of optical fiber taper and its impact on image contrast were analyzed.<sup>7</sup> The impact of lens-coupling efficiency on signal-to-noise ratio was investigated.<sup>8</sup> This communication focuses on the geometrical distortions caused by relay lenses, since it is well known that aberrations, including geometrical distortions, do exist even with a well-designed and well-built lens. We will first introduce the origin of lens geometrical distortion. We will then take the lens-coupled CCD x-ray imaging system as an example to analyze the positional errors introduced by lens geometrical distortion. Finally, we will present an algorithm for correcting geometrical distortions caused by lens in digital x-ray imaging.

## II. GEOMETRICAL DISTORTIONS CAUSED BY LENS

As shown by Fig. 1, a relay lens used in an optically coupled CCD x-ray imaging system collects light from a

point on a scintillator, and focuses it onto a corresponding conjugate point on an electronic imager. Under the most practical conditions, the lens, same as all other optical components, is not able to form a perfect image due to the presence of aberrations. Lens aberrations include spherical aberration, coma, field curvature, astigmatism, axial color, lateral color, and distortion.<sup>9</sup> Most of these aberrations degrade the image quality by "blurring" the image.

Lens distortion is a unique aberration in that it does not degrade the quality of the image in terms of sharpness and focus. Rather, it affects the shape of the image, causing it to depart from a true-scaled duplication of the original object. For instance, if one acquires the image of a square grid as shown in Fig. 2(a), the recorded image can be affected by pincushion distortion, as shown in Fig. 2(b), and affected by barrel distortion, as shown in Fig. 2(c). Pincushion is an outward displacement of a given image point from its desired location on a mean image plane: Its magnitude increases, in the simplest cases, as the field angle of the optical system increases. The field angle  $\alpha$  is defined in Fig. 1. On the other hand, barrel distortion is an inward displacement, and its magnitude also increases with the field angle, but with a different orientation [see Fig. 2(c)]. The distortions demonstrated in Fig. 2 are only radial distortions, which for a purely rotational system cause the actual image point to be displaced radially in the image plane, independent of the azimuth in the field.



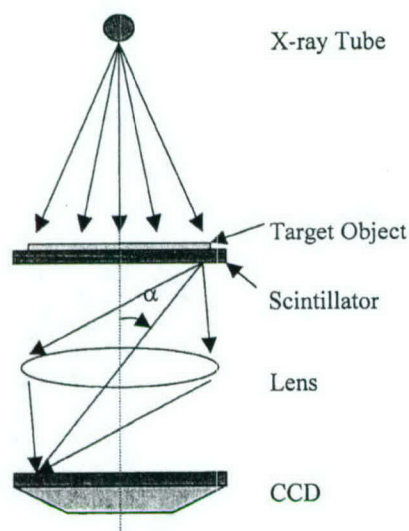


FIG. 1. A schematic of a lens-coupled CCD digital x-ray imaging system. The field angle  $\alpha$  is defined as the angle formed by the optical axis (dotted line) and the principal ray through the center of the lens connecting the two conjugate points.

In principle, a lens is a rotationally symmetric system. In practice, no ideal lenses can be made. Small errors retained in the alignment and centering of a multielement optical system lead to tangential displacement of image point; the magnitude of such distortion depends on both the azimuth and the off-axis position of the field. Figure 3 shows an example of the tangential distortion. One of the effects of tangential distortion is that a straight line passing through the center of the field may be recorded as a weakly curved line.

Lens aberrations cannot be avoided completely in optical design; however, they can be minimized. Optical designers evaluate the potential contribution of each aberration to the final system performance and adjust the configuration of the optical assembly to achieve satisfactory performance for each application. For instance, an optical designer usually balances the outward and inward displacements to minimize geometrical distortions. The designer, however, has to "trade-off" many factors, such as cost and size, against technical parameters required by specific applications. With exception of certain custom built systems, distortion errors in the range of 1–3 percent may be present in commercially available relay lenses, when these lenses are used in the imaging system.

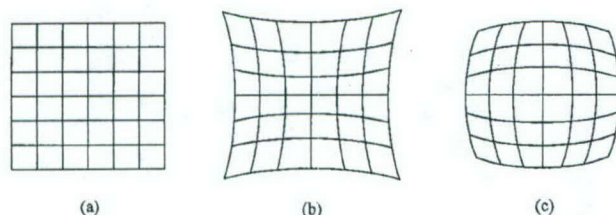


FIG. 2. Illustration of geometrical distortions introduced by lens. (a) A checkerboardlike grid without distortion; (b) Pincushion distortion; (c) Barrel distortion.

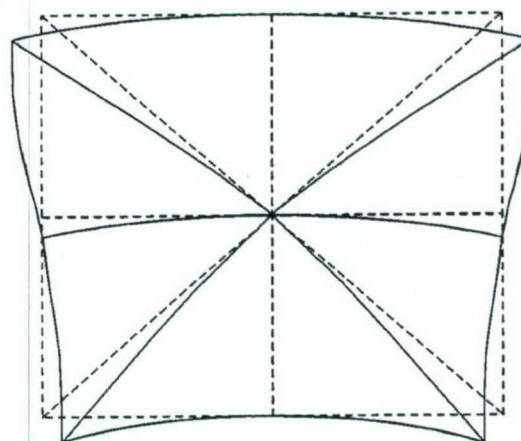


FIG. 3. Illustration of tangential distortion: A straight line passing through the center (optical axis) of the field is recorded as a weakly curved line. In this schematic, the dashed lines show the undistorted geometrical pattern and the solid lines represent the distorted pattern.

Due to the presence of the residual distortion, the local scale on an image produced by a lens-coupled digital x-ray imaging system may vary both radially and tangentially at a given image position from the mean value.

In many diagnostic-imaging applications, such as routing gastrointestinal fluoroscopy, the presence of geometrical distortions is often unnoticed by the image readers (its effect on the diagnostic quality is up to discussion). The presence of geometrical distortions is, however, of great importance in position-dependent, quantitative imaging, such as in cardiac catheter placement, neurological embolization procedures, and in image guided biopsy. For instance, the errors introduced by both radial and tangential distortions reduce the positional accuracy of a lens-coupled CCD stereotactic system.

### III. POSITIONAL ERROR INTRODUCED BY LENS

To investigate the geometrical distortion introduced by lenses in digital x-ray imaging, a lens-coupled CCD prototype was used.<sup>3</sup> The system, consisting of a scintillating screen ( $\text{Gd}_2\text{O}_2\text{S:Tb}$ ), a relay lens and a CCD camera, is attached to a clinical x-ray machine. The camera employs a mechanical shutter. An optical hood was used to shield the CCD sensor from ambient light. The CCD array size is  $1024 \times 1024$  pixels, and  $0.024 \text{ mm} \times 0.024 \text{ mm}$  per pixel. The camera was operated under a temperature of  $-25^\circ\text{C}$  to reduce thermal electron noise. The low temperature was achieved with a compact thermoelectric cooler. The operation of the system is described as follows: (1) During x-ray exposure, the x-ray beam passing through the testing target is attenuated and interacts with the scintillating screen. (2) The x-ray photons are then converted into a large number of visible light photons. (3) The relay lens projects the optical scene from the scintillating screen to the photosensitive surface of the CCD camera. (4) The CCD pixel array samples the information and creates a digital image. In our experi-



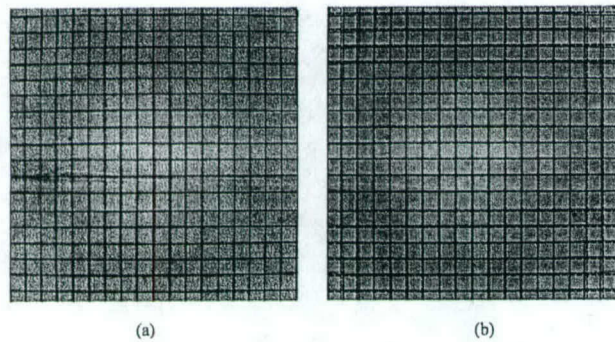


FIG. 4. Digital x-ray images showing the effect of lens distortion. (a) An x-ray image of a checker board like grid, acquired using a prototype lens-coupled CCD x-ray imaging system, (b) a standard map of the grid (dashed lines), properly scaled, was artificially overlaid on the distorted x-ray image, to demonstrate the geometrical distortion.

ment, this operation was controlled by a computer. The x-ray energy and exposure used in the experiments were 30 kVp and 32 mAs, respectively.

A commercial Nikon lens, F/1.2, 50 mm focal length, equipped with a close-up (Nikon Close-up #2) lens was used as the relay lens to project the optical image from the scintillating screen to the CCD imager. The relay lens is working at a 3.6:1 demagnification ratio, thus making an object of one millimeter in length occupy  $\sim 11.6$  pixels in digital image. During experiments, a checkerboard-like grid made by copper wires was imaged by the prototype system. To minimize the effect of x-ray focal spot on image quality and geometrical shape, the copper wires were kept directly against the scintillator (no air gap between the testing target and the x-ray detector), and the distance from the x-ray focal spot to the scintillator was kept at 650 mm. The diameter of the copper wires was 0.17 mm and the spacing between the copper wires (center to center) was 5 mm.

An x-ray image of the calibration grid acquired by our imaging system is shown in Fig. 4(a). In Fig. 4(b), a map of the grid (dashed lines), properly scaled, is artificially overlaid over the acquired image, to demonstrate the geometrical distortion. At locations near the center of the image (near the optical axis of the lens), the standard map overlaps with the x-ray image almost perfectly. At locations toward the edges of the image, the displacement between the map and the x-ray image becomes clearly noticeable. Apparently, this specific lens used in this prototype introduced a significant barrel distortion.

To quantitatively measure positional errors introduced by lens distortions in digital x-ray imaging, positional displacement of the grid image from its true location was calculated for all the feature points (intersections of the grid wires). In

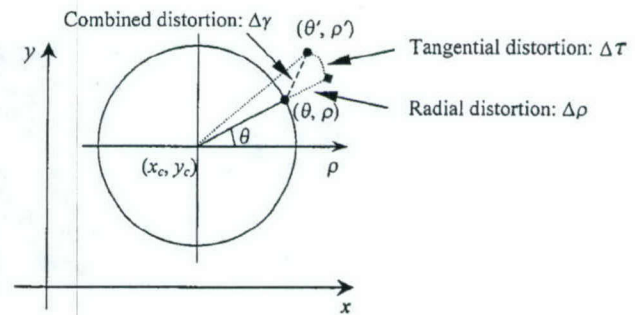


FIG. 5. Illustration of the coordinate system to characterize lens distortions. The optical center  $(x_c, y_c)$  is served as the origin of polar domain. The base axis of the polar system is parallel to the  $x$  axis of Cartesian system. The distorted and undistorted points are denoted as  $(\rho, \theta)$  and  $(\rho', \theta')$ , respectively. The radial distortion,  $\Delta\rho$ , tangential distortion,  $\Delta\tau$ , and combined distortion,  $\Delta\gamma$ , are also illustrated in this figure.

Table I, radial distortion errors, and total distortion errors (combined radial and tangential errors) are listed as functions of the field angle of the optical system. The radial distortion error,  $\Delta\rho$ , and the total distortion error,  $\Delta\gamma$ , are illustrated in Fig. 5 in a polar coordinate.

As shown in Table I, the positional displacement of an object imaged by such a lens-coupled digital x-ray imaging system can be, in the most severe cases, more than nine pixels away from its true location within a field angle of  $30^\circ$ . Considering the fact that the CCD imager used in the prototype has only  $1024 \times 1024$  pixels, the positional error introduced by the lens distortion cannot be neglected in any position-dependent, quantitative x-ray imaging.

#### IV. AN ALGORITHM FOR LENS DISTORTION CORRECTION

Digital image processing techniques can be used to correct geometrical distortions introduced by optical and optoelectronic components.<sup>10-12</sup> In our study, a correction algorithm was introduced to minimize the lens distortion. The algorithm was derived based on the nature of the lens distortion.

After a digital image of a standard grid is acquired by the imaging system, the algorithm operates as follows:

- (1) Localize the intersections of the wires of the grid (feature points);
- (2) Create an ideal map of the grid;
- (3) Identify the optical center of the lens;
- (4) Perform polynomial-transformation to correct distortions.

TABLE I. Positional errors introduced by relay lens versus field angle of the optical system.

Field angle $\alpha$ (degree)	3.6	8.6	13.0	17.4	22.1	26.2	30.0
Radial distortion $\Delta\rho$ (pixel)	1.26	2.28	3.25	4.30	5.43	6.94	7.42
Combined distortion $\Delta\gamma$ (pixel)	2.39	3.16	4.15	5.19	6.61	8.04	9.71
Combined distortion $\Delta\gamma$ (mm)	0.20	0.27	0.36	0.45	0.57	0.69	0.84



These procedures are discussed in detail in the succeeding text.

### A. Localizing feature points

A semiautomatic procedure was developed to localize the positions of the feature points (wire intersections of the grid). The first step of this procedure was to manually locate two adjacent feature points, which served as the starting points of the semiautomatic procedure.<sup>13</sup> Centered at each of the starting points, a local window was set up ( $40 \times 40$  pixels rectangle in our experiment). A connected region was determined that contained  $m$  adjacent pixels ( $m=8$  in our experiment) with the lowest gray levels inside the window. This region could be named as a valley region. Because of the superposition of the two wires, the x-ray attenuation at each intersection of the grid (feature point) was higher. Therefore, feature points showed minimum pixel value in the image. It is reasonable to assume that the feature point was located inside the valley region. The reason for chosen a connected region instead of a pixel is to improve the algorithm's robustness for the unavoidable imaging noise, and to improve the accuracy of the locations of the feature points. The exact location of the feature point  $(x_a, y_a)$  was defined as the gravity center of the valley region

$$x_a = \frac{1}{m} \sum_{i=1}^m x_i f(x_i, y_i)$$

$$y_a = \frac{1}{m} \sum_{i=1}^m y_i f(x_i, y_i), \quad (1)$$

where  $f(x_i, y_i)$  was the gray level at point  $(x_i, y_i)$  in the valley region.<sup>14,15</sup> Using Eq. (1), the first two feature points, their starting points being manually located, can be determined in sub-pixel accuracy.

The algorithm could identify the next starting point according to the distance between two known feature points along the extension (or perpendicular) line between them, since the calibration image was a checkerboardlike grid. One by one, the remaining feature points were determined by using this method.

### B. Creating the ideal map of the grid

The ideal map of the grid was created to serve as the standard pattern for image correction. In Ref. 16, Shah and Aggarwal acquired an ideal image by another lens that introduced minimal distortion. If the polynomial warping method was employed, the grid target could be used as an undistorted ideal grid itself.<sup>16</sup> Here, a method was employed to create an ideal map of the grid from the actual distorted grid image using the following mechanism.

The grid pattern consisted of two sets of parallel straight lines intersecting at a right angle. One set of parallel lines can be described by the equation:

$$y_i = kx + ib \quad (i = \dots -1, 0, 1, \dots), \quad (2)$$

where the parameters  $k$  and  $b$  are the slope and the  $y$ -separation of the lines, respectively. It is reasonable to as-

sume that the lens distortion is negligible near the center of the image. Thus, the parameters  $k$  and  $b$  can be estimated using feature points in the center region of the actual grid image. In our experiment, with the whole image size of  $1024 \times 1024$  pixels, a  $200 \times 200$ -pixel sub-image was taken around the image center for the purpose of the parameter calculation. This sub-image covers four pairs of straight lines. Each line equation was initially determined using two calculated feature points as described above. Then in the perpendicular direction along this line, the points with a local minimum gray level were localized. Using the least mean-square fitting method, the parameters of the line equation could be determined precisely with these local minimum gray level points. The calculated grid map of the center region was then extended to the whole image, thereby creating the entire calculated grid map. However, the map was roughly positioned with respect to the geometrical center of the x-ray image array. The last step of this procedure was, therefore, to shift the calculated grid map slightly to achieve the best alignment with the actual grid image by minimizing the following criterion function

$$F = \sum_i [(x_{gi} - x_{ai})^2 + (y_{gi} - y_{ai})^2], \quad (3)$$

where  $(x_g, y_g)$  and  $(x_a, y_a)$  are the feature points corresponding to the calculated grid map and actual grid image, respectively. The subscript  $i$  indicates the  $i$ th feature point, and the summation in Eq. (3) is over all feature points of the x-ray image.

### C. Identifying the optical center of the lens

Normally, the lens distortion is mainly in radial direction, which causes an inward or outward displacement of a given image point from its true location. This type of distortion is strictly symmetric about the optical axis.<sup>17-19</sup> With this property, a method was developed to localize the optical center (optical axis).

Let  $(x_c, y_c)$  denote the optical center, the radial distortion at any feature point  $(x_{ai}, y_{ai})$  in the actual image can be calculated by:

$$d(x_{ai}, y_{ai}) = \sqrt{(x_{ai} - x_c)^2 + (y_{ai} - y_c)^2} - \sqrt{(x_{gi} - x_c)^2 + (y_{gi} - y_c)^2}, \quad (4)$$

where,  $(x_{gi}, y_{gi})$  is the corresponding feature point to the  $(x_{ai}, y_{ai})$  in the calculated ideal grid map.

For feature point  $(x_{ai}, y_{ai})$ , its symmetric location about the optical center  $(x_c, y_c)$  is given by  $(2x_c - x_{ai}, 2y_c - y_{ai})$ . Therefore, the asymmetry of the radial distortion to  $(x_c, y_c)$  can be characterized by a function

$$J(x_c, y_c) = \sum_i [d(x_{ai}, y_{ai}) - d(2x_c - x_{ai}, 2y_c - y_{ai})], \quad (5)$$

where the subscript  $i$  indicates the  $i$ th feature point. The summation is over all feature points of the x-ray image. The optical center is such a point that the asymmetry of the distortion is at a minimum level. Therefore, the problem of



searching the exact location of the optical center is equivalent to an optimization procedure in which the center position  $(x_c, y_c)$  is to be determined in order to minimize the object function  $J$  in Eq. (5).

To perform such an optimization procedure, the following steps were adopted:

- (1) First, select the center of the digital image as the initial location for the optical center.
- (2) Search for  $x_c$ , by minimizing the object function  $J$  in Eq. (5) with  $y_c$  fixed.
- (3) Then, with a fixed  $x_c$  determined in step 2, search for  $y_c$  by minimizing  $J$ .
- (4) Repeat steps 2 and 3 until the location of the optical center is stabilized within a reasonable tolerance (0.2 pixels in our experiment).

It should be noted that for a feature point  $(x_a, y_a)$ , its symmetric point  $(2x_c - x_a, 2y_c - y_a)$  about the center  $(x_c, y_c)$  may be falling between the known grid wire intersections. In such a situation, a two-dimensional interpolation was implemented according to its neighbors to seek an estimate of its radial distortion. Bilinear interpolation was used in our method.<sup>20</sup>

#### D. Performing polynomial-transform to correct distortion

Polynomial transformation is a common method used to correct the distortions.<sup>21-23</sup> Since a combination of radial distortion and tangential distortion was seen in the image, in our experiment two sets of polynomials were needed. One was used to correct the radius as measured from the optical center, and the other was used to correct the polar angle as measured from the base axis of the polar system. As shown in Fig. 5, the distorted image of a feature point is denoted as polar coordinate  $(\rho, \theta)$ , and the distortion-free image of the point is denoted as  $(\rho', \theta')$ . The radial position of each pixel and the tangential offset component were corrected by applying two set of  $N$ -order polynomials:

$$\begin{aligned}\theta' &= a_1\theta + a_2\theta^2 + a_3\theta^3 + a_4\theta^4 + \dots, \\ \rho' &= b_1\rho + b_2\rho^2 + b_3\rho^3 + b_4\rho^4 + \dots,\end{aligned}\quad (6)$$

where,  $a_i$  and  $b_i$  are the distortion coefficients. The above equations hold for all feature points of the image. Because the number of feature points generally exceeded the number of polynomial coefficients,  $a_i$  and  $b_i$  were solved by least-squares fitting which minimized the mean-square error between the calculated positions from Eq. (6) and the undistorted positions in ideal grid map. The two sets of coefficient  $a_i$  and  $b_i$  can be used for the corrections of all image signals.

### V. RESULTS AND DISCUSSIONS

#### A. Effectiveness of the algorithm

This algorithm was applied to the images acquired by our prototype lens-coupled digital x-ray imaging system. The corrected images in Fig. 6 showed a significant distortion

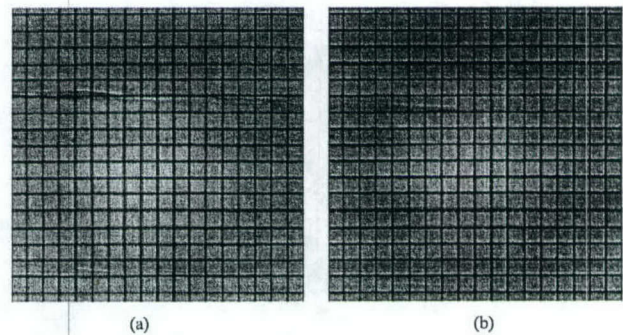


FIG. 6. Digital x-ray images showing the effect of distortion. (a) The corrected result of the grid image by fourth-order polynomials (see the image of the grid before the correction in Fig. 4). The mean residual error was reduced from 8.04 pixel to 1.78 pixel. (b) A standard grid map (dashed lines) was overlaid on the corrected grid image to show the minimized geometrical distortion. Compare with Fig. 4 to see the effect of the correction.

reduction when compared with the uncorrected images in Fig. 4.

To quantitatively measure the effectiveness of the correction algorithm, the absolute mean residual error (positional displacement of the grid image from its true location) was calculated for all of the intersections of the grid wires. The mean residual error before correction was 8.04 pixels and after corrections 1.78 pixels. In Fig. 7, the mean values of the radial distortion error,  $\Delta\rho$ , before and after correction are plotted as function of the field angle  $\alpha$  of the optical system (refer to Fig. 1 for the definition of  $\alpha$ ). In Fig. 8, the mean values of the combined distortion error,  $\Delta\gamma$ , before and after correction, are also plotted versus the field angle  $\alpha$  (refer to Fig. 5 for illustration of  $\Delta\rho$  and  $\Delta\gamma$ ).

Clearly, the polynomial algorithm effectively corrected the lens distortion in digital x-ray imaging.

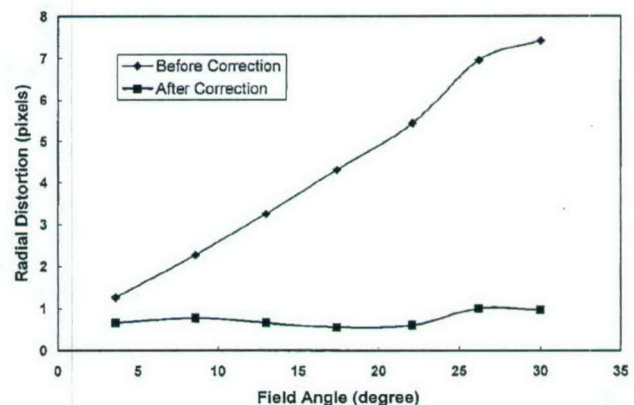


FIG. 7. The mean radial distortion errors before and after correction as a function of field angle of the optical system. Before the correction, the error ranges from 1.26 pixels (0.109 mm) to 7.42 pixels (0.64 mm). After correction, the mean error ranges from 0.56 pixels (0.05 mm) to 1.00 pixels (0.086 mm).



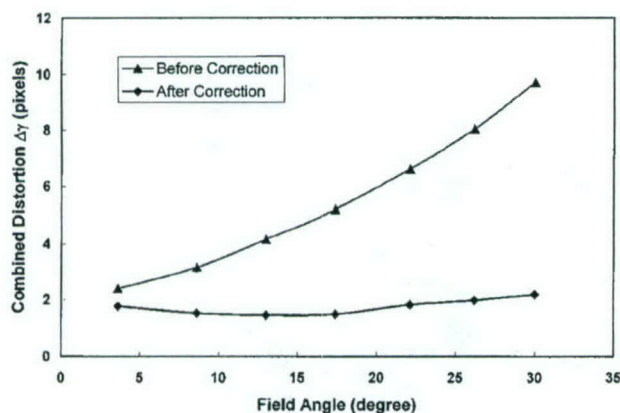


FIG. 8. The combined distortion errors  $\Delta\gamma$  with respect to field angle before and after correction (refer to Fig. 5 for the definition of  $\Delta\gamma$ ). Before the correction, the error ranges from 2.39 pixels (0.206 mm) to 9.71 pixels (0.84 mm). After correction, the error ranges from 1.45 pixels (0.125 mm) to 2.18 pixels (0.19 mm).

### B. Order of polynomials and its impact on distortion correction

As described previously, two sets of  $N$ -order polynomials were used in correcting both radial and tangential distortions. It is important to select a proper order of  $N$  to achieve optimized result. Theoretically, higher-order polynomial leads to less residual error. However, higher-order polynomials can also cause oscillation and make the mathematical solutions unstable. In our experiments, the effect of different orders of the polynomials on lens distortion correction was tested by generating sets of coefficients for orders:  $N=2, 3, 4, 5, 6$ . The mean residual errors after correction for different  $N$  values are listed in Table II. The results showed that the image correction improved as the order of the polynomial increased up to four. However, the correction effect decreased with higher-order polynomials.

In addition to the possible oscillation, another reason for lack of improvement was that it could lead to some extra round-off errors when the higher order polynomial transformation was performed. For the investigations using our imaging system, the optimal order of polynomials appeared to be four. The corresponding polynomial coefficients  $a_i$  and  $b_i$  are listed in Table III.

## VI. CONCLUSION

Optical coupling is an important link in various digital x-ray imaging systems. The optical properties of the components, either a lens, a fiber bundle or other optoelectronic device will affect the quality of clinical procedures significantly. There is no ideal optical component or optoelectronic

TABLE II. The mean residual errors of corrected image using polynomial transformation of different orders.

Polynomial order ( $N$ )	2	3	4	5	6
Mean residual error (Pixel)	2.14	2.02	1.78	3.94	4.77
Mean residual error (mm)	0.18	0.17	0.15	0.34	0.41

TABLE III. The polynomial coefficients used for correcting lens distortions ( $N=4$ ).

For radial	$a_1$	$a_2$	$a_3$	$a_4$
Distortion	1.008	$2.836 \times 10^{-5}$	$-1.634 \times 10^{-7}$	$1.091 \times 10^{-10}$
For tangential	$b_1$	$b_2$	$b_3$	$b_4$
Distortion	1.003	$-2.293 \times 10^{-4}$	$-4.751 \times 10^{-4}$	$3.074 \times 10^{-5}$

device that can relay an image without degrading its quality or distorting its shape. One could, however, balance the design trade-offs of the selected components according to the specific clinical applications.

Arguably, optical lens still is the most conventional and widely used imaging component. In comparison with many other optical techniques, lenses have many advantages, such as (1) cost effectiveness: It may be expensive to build just one or two custom lenses, but in mass production, lenses can be made at very low cost; (2) flexibility: Even with a simple relay lens, the parameters such as magnification, aperture, field of coverage, and depth of focus are adjustable; (3) image quality: A well-designed lens offers much higher spatial resolution than many other optical components or optoelectronic devices. For most commercial and custom lenses, aberrations are selectively minimized according to the specific applications. However, residual aberrations, including geometrical distortions do exist even with a well-designed and well-built lens. Although these residual distortions are usually small in terms of absolute or relative errors, they will reduce, for instance, the positional accuracy of image guided procedures.

The distortion introduced by relay lenses, however, can be minimized with digital image processing techniques. In fact, it is easier to correct distortions introduced by lenses than that by many other types of imaging components, since lens distortion is primarily radial and tangential dependant.<sup>24-27</sup> In other words, lens distortion may be "mapped" with a set of mathematical formulas and compensated accordingly using appropriate algorithms, as demonstrated in this paper.

We have shown that based on the nature and the classifications of lens distortion, the coefficients of the polynomial in the correction algorithm can be determined to minimize both radial and tangential distortions. For the specific imaging system investigated, the fourth order polynomials provided the best correction results. The low order polynomials were not sufficient for modeling the lens distortion, and the higher order polynomials tended to introduce oscillation that makes the algorithm unstable.

Overall, our analysis suggests that lens distortion should be considered in developing optically coupled digital x-ray imaging systems for position-dependant, quantitative x-ray imaging, and that residual geometrical distortions could be minimized effectively using digital image processing techniques. The advantages of using lens to relay images from scintillating screen to electronic imager are cost effectiveness, flexibility and image quality.



## ACKNOWLEDGMENTS

This work was supported in part by a NIH-NCI grant (Grant No. CA 70209) (P.I.: H Liu) and by a U.S. Army breast cancer research Grant No. DAMD 17-97-1-7138 (P.I.: H Liu).

<sup>a</sup> Author to whom correspondence should be addressed. Telephone: (410) 614-9291; Fax: (410) 614-7760. Electronic mail: hliu@jhim.edu

<sup>1</sup> A. Karellas, L. Harris, H. Liu, M. Davis, and C. D'Orsi, "Charge-Coupled Device detector: Performance considerations and potential for mammographic imaging," *Med. Phys.* **19**, 1015-1023 (1992).

<sup>2</sup> H. Liu, J. Xu, G. Halama, and J. McAdoo, "Digital fluoroscopy using an optically coupled CCD: Preliminary investigations," *SPIE Proceedings* **2976**, 256-261 (1997).

<sup>3</sup> A. Jalink, J. McAdoo, G. Halama, and H. Liu, "CCD-mosaic technique for large field digital mammography," *IEEE Trans. Med. Imaging* **15**, 260-267 (1996).

<sup>4</sup> H. Liu, L. L. Fajardo, J. R. Barrett, and R. A. Baxter, "Contrast-detail detectability analysis: comparison of a digital spot mammography system and an analog screen-film mammography system," *Acad. Radiol.* **4**, 197-203 (1997).

<sup>5</sup> H. Liu, L. L. Fajardo, and B. Penny, "Signal-to-noise ratio, noise power spectrum and detective quantum efficiency analysis of optically coupled CCD mammography imaging systems," *Acad. Radiol.* **3**, 799-805 (1996).

<sup>6</sup> H. Liu, A. Karellas, S. Moore, and L. Harris, "Lesion detectability considerations for an optically coupled CCD x-ray imaging system," *IEEE Trans. Nucl. Sci.* **41**, 1506-1509 (1994).

<sup>7</sup> H. Liu, A. Karellas, L. Harris, and C. D'Orsi, "Optical properties of fiber tapers and their impact on the performance of a fiber optically coupled CCD x-ray imaging system," *SPIE Proceedings* **1894**, 136-147 (1993).

<sup>8</sup> H. Liu, A. Karellas, and L. Harris, "Methods to calculate lens coupling efficiency in an optically coupled CCD x-ray imaging system," *Med. Phys.* **21**, 1193-1195 (1994).

<sup>9</sup> B. H. Walker, "Primary lens aberrations," in *Optical engineering fundamentals* (SPIE Optical Engineering Press, Bellingham, Washington, 1998), pp. 129-148.

<sup>10</sup> J. M. Boone, J. A. Seibert, W. A. Barrett, and E. A. Blood, "Analysis and correction of imperfections in the image-intensifier-tv-digitizer imaging chain," *Med. Phys.* **18**, 236-242 (1991).

<sup>11</sup> R. Ning, J. K. Riek, and D. L. Conover, "An image intensifier based volume tomographic angiography imaging system: geometric distortion correction," *SPIE Proceedings* **2163**, 199-210 (1994).

<sup>12</sup> B. Achueler and X. Hu, "Correction of image intensifier distortion for three-dimensional x-ray angiography," *SPIE Proceedings* **2432**, 272-279 (1996).

<sup>13</sup> E. Gronenschild, "The accuracy and reproducibility of a global method to correct for geometric image distortion in the x-ray imaging chain," *Med. Phys.* **24**, 1875-1888 (1997).

<sup>14</sup> E. L. Hall, *Computer Image Processing and Recognition* (Academic, New York, 1979), pp. 185-189.

<sup>15</sup> K. R. Castleman, *Digital image Processing* (Prentice Hall, Upper Saddle River, New Jersey, 1996), pp. 120-127.

<sup>16</sup> S. Shah and J. Aggarwal, "Intrinsic parameter calibration procedure for a (high distortion) fish-eye lens camera with distortion model and accuracy estimation," *Pattern Recogn.* **29**, 1775-1788 (1996).

<sup>17</sup> Lasmea, "Camera Calibration from Spheres Images," *Proceedings of Computer Vision-ECCV'94*, Stockholm, Sweden (Springer-Verlag, Berlin, 1994), pp. 449-454.

<sup>18</sup> D. C. Brown, "Close-range camera calibration," *Photogramm. Eng. Remote Sens.* **37**, 855-866 (1971).

<sup>19</sup> *Manual of Photogrammetry*, 4th ed. (Amer. Soc. Photogrammetry, Falls Church, Virginia, 1980).

<sup>20</sup> D. Ballard and C. Brown, *Computer Vision* (Prentice-Hall, Inc., Englewood Cliffs, New Jersey, 1982).

<sup>21</sup> J. Weng, P. Cohen, and M. Hernion, "Camera calibration with distortion models and accuracy evaluation," *IEEE Trans. On PAMI-14*, No. **10**, 965-980 (1992).

<sup>22</sup> Z. Jericevic, D. M. Benson, J. Bryan, and L. C. Smith, "Geometric correction of digital images using orthonormal decomposition," *J. Microsc.* **149**, Pt.3 233-245 (1988).

<sup>23</sup> R. Fahrig, M. Moreau, and D. M. Holdsworth, "Three-dimensional computed tomographic reconstruction using a C-arm mount XR21: correction of image intensifier distortion," *Med. Phys.* **24**, 1097-1106 (1997).

<sup>24</sup> D. C. Brown, "Decentering distortion of lenses," *Photogramm. Eng. Remote Sens.* **32**, 444-462 (1966).

<sup>25</sup> R. Y. Tasi, "A versatile camera calibration technique for high-accuracy 3D machine vision metrology using off-the-shelf TV cameras and lenses," *IEEE Journal of Robotics and Automation* **3**, 323-344 (1987).

<sup>26</sup> Y. Nomura, M. Sagara, H. Naruse, and A. Ide, "Simple calibration algorithm for high-distortion-lens camera," *IEEE Trans. On PAMI-14*, No. **11**, 1095-1099 (1992).

<sup>27</sup> H. Bacakoglu and M. S. Kamel, "A three-step camera calibration method," *IEEE Trans. Instrum. and Measurement* **46**, 1165-1172 (1997).



# Noise power spectra of images from digital mammography detectors

Mark B. Williams,<sup>a)</sup> Peter A. Mangiafico, and Piero U. Simoni  
*Department of Radiology, University of Virginia, Charlottesville, Virginia 22908*

(Received 9 September 1998; accepted for publication 12 April 1999)

Noise characterization through estimation of the noise power spectrum (NPS) is a central component of the evaluation of digital x-ray systems. We begin with a brief review of the fundamentals of NPS theory and measurement, derive explicit expressions for calculation of the one- and two-dimensional (1D and 2D) NPS, and discuss some of the considerations and tradeoffs when these concepts are applied to digital systems. Measurements of the NPS of two detectors for digital mammography are presented to illustrate some of the implications of the choices available. For both systems, two-dimensional noise power spectra obtained over a range of input fluence exhibit pronounced asymmetry between the orthogonal frequency dimensions. The 2D spectra of both systems also demonstrate dominant structures both on and off the primary frequency axes indicative of periodic noise components. Although the two systems share many common noise characteristics, there are significant differences, including markedly different dark-noise magnitudes, differences in NPS shape as a function of both spatial frequency and exposure, and differences in the natures of the residual fixed pattern noise following flat fielding corrections. For low x-ray exposures, quantum noise-limited operation may be possible only at low spatial frequency. Depending on the method of obtaining the 1D NPS (i.e., synthetic slit scanning or slice extraction from the 2D NPS), on-axis periodic structures can be misleadingly smoothed or missed entirely. Our measurements indicate that for these systems, 1D spectra useful for the purpose of detective quantum efficiency calculation may be obtained from thin cuts through the central portion of the calculated 2D NPS. On the other hand, low-frequency spectral values do not converge to an asymptotic value with increasing slit length when 1D spectra are generated using the scanned synthetic slit method. Aliasing can contribute significantly to the digital NPS, especially near the Nyquist frequency. Calculation of the theoretical presampling NPS and explicit inclusion of aliased noise power shows good agreement with measured values. © 1999 American Association of Physicists in Medicine. [S0094-2405(99)00707-5]

Key words: noise power spectrum, digital mammography, detector, image analysis

## I. INTRODUCTION

The signal-to-noise ratio imposes the fundamental limitation to object perceptibility in a digital radiograph because image contrast can be manipulated during the display of digitally acquired radiographic images. Thus, noise characterization plays an increasingly central role in the evaluation of system performance in medical imaging. Well-developed methods used for noise characterization in film-based systems are currently being reassessed and reformulated to accommodate both the different nature of the noise and to take advantage of the analytical tools available with digital processing. An indication of both the current interest level and lack of consensus regarding noise characterization is the recent establishment of an AAPM Task Group (No. 16) for Standards for Noise Power Spectrum Analysis.

The noise power spectrum (NPS) is a spectral decomposition of the variance. As such, the NPS of a digital radiographic image provides an estimate of the spatial frequency dependence of the pixel-to-pixel fluctuations present in the image. Such fluctuations are due to the shot (quantum) noise in the x-ray quanta incident on the detector, and any noise introduced by the series of conversions and transmissions of quanta in the cascaded stages between detector input and output. Examples of the latter are gain variances in the con-

version of x-ray quanta to light quanta in a phosphor (or to electron-hole pairs in a solid-state detector), statistical fluctuations in the transmission of optical quanta between a scintillator and a photodetector, and additive noise sources such as preamplifier noise. The NPS is a much more complete description of image noise than is quantification of integrated (total) noise via simple measurement of the rms pixel fluctuations, because it gives information on the distribution in frequency space of the noise power. An understanding of the frequency content of image noise can provide insight regarding its clinical impact. For example, in mammography, excess high-frequency noise may render the detection of microcalcifications impossible. If desired, the total variance can be obtained by integrating the NPS over spatial frequency.

In this paper we discuss aspects of NPS estimation as applied to digital radiographic systems. We begin with a general review of pertinent definitions and relations, and discuss the most important considerations when applying spectral estimation techniques to digital radiographic systems. Mathematical derivations sufficient to provide the reader with tools for quantitative application of the concepts are given, with more detailed development available in the cited references. These techniques are then applied to the analysis



of the noise properties of two developmental detectors for full-field digital mammography using charge coupled devices (CCDs).

## II. BACKGROUND

Linear systems analysis can be usefully applied to any radiographic system whose transfer characteristic between input and output is *linear* (or linearizable) and *stationary* (the transfer properties are independent of location at the input surface).<sup>1,2</sup> In this formalism, signal and noise are typically decomposed into their Fourier components (although other bases can be used), and input and output relations are expressed in terms of the frequency space Fourier amplitudes. Digital radiographic systems such as the one considered here usually exhibit linear responses to the incident x-ray fluence over several orders of magnitude. The following analysis assumes that the detector is operated within its linear range. For the digital mammography systems whose noise characterization is reported here, care was taken to first determine the linear range of operation for each. The range of exposures used for the NPS estimates in this paper fall well within the boundaries of linear operation. In a digital detector the analog (presampling) signal and noise propagated through the detector are sampled by the digital matrix at discrete points. Therefore, the system response is not strictly shift invariant (unless shifts are by an integer number of pixels). The effects of digital sampling on the NPS are described below.

A random process such as the noise fluctuations in an image is considered (wide-sense) *statistically stationary*, if its autocorrelation function (see below) is independent of the particular data sample (e.g., the particular location in the image) used to obtain it. This is only strictly true in a radiographic image if (a) noise samples are obtained from spatially uniform exposures, and (b) the detector adds no spatially fixed correlated noise. Dobbins has shown that the presence of a deterministic signal in the image data used to estimate the NPS has no effect on the resultant spectral estimates.<sup>3</sup> One other important assumption concerning the noise is whether or not it is *ergodic*. The noise in an image is ergodic if expectation values (averages) obtained from data samples at various locations in the image are equivalent to ensemble averages obtained from repeated measurements under identical conditions at a single location. Ergodicity implies stationarity, but not necessarily vice versa. The assumption of ergodicity of the noise in radiographic images made under conditions of uniform irradiation is typically made, and permits averaging of spectra obtained from several areas of the image. Strictly speaking, even under conditions of

nominally uniform irradiation, factors such as the heel effect result in deviation from true ergodicity. For this reason, it is often best to estimate the NPS from a common, limited area of a series of images, rather than from a large portion of a single image. In the work described here, data used for a given spectral estimate were obtained from a series of images, but using an area located at a fixed distance from the chest wall edge.

In a cascaded system such as a digital mammography detector, the output of one stage constitutes the input to the following stage. In a linear, shift invariant cascaded system, each of the independent stages are also linear and shift invariant. At the output of any given stage of a cascaded detector system, the minimum possible value of the NPS is that set by the (uncorrelated) Poisson variance of the output quanta, which is equal to the number of quanta. Building on the work of Rossmann<sup>4</sup> and Kemperman and Trabka,<sup>5</sup> Rabhani, Shaw, and Van Metter have developed expressions for the propagation of the NPS through cascaded linear systems.<sup>6</sup> Using moment generating functions, they show that noise generated during a stochastic amplification process in one stage (such as the conversion of a single absorbed x-ray photon to many light photons) is effectively passed as signal to the subsequent stage. Furthermore, they show that in a stochastic scattering process, while correlated components of the NPS are reduced by the square of the modulation transfer function (MTF) associated with the blurring process, uncorrelated Poisson noise is transferred independently of the MTF. This *stochastic* type of blur has a different effect on the NPS than *deterministic* blur, in which both correlated and uncorrelated components of the NPS of the preceding stage are attenuated by the square of the blur MTF.<sup>7</sup> Deterministic blur does not degrade the signal-to-noise ratio because the signal is also modulated by the blur MTF. Visible photon scatter in a phosphor is an example of stochastic blur; the effect of the integrating aperture of the individual pixels in a digital system is an example of deterministic blur.

### A. Direct and indirect methods of NPS calculation

The NPS is defined as the Fourier transform (FT) of the autocorrelation function, defined in one dimension as<sup>8</sup>

$$C(x) = \lim_{L \rightarrow \infty} \frac{1}{L} \int_{-L/2}^{L/2} p(x+\tau) p^*(\tau) d\tau, \quad (1)$$

where  $p(x)$  is the value (pixel value for a digital image) of the one-dimensional image (1D) at position  $x$ , and  $p^*(x)$  is its complex conjugate. Since  $p(x)$  is real,  $p(x) = p^*(x)$ . The Fourier transform of  $C(x)$  is then

$$\begin{aligned} S(u) &= \int_{-\infty}^{\infty} C(x) e^{-2\pi i x u} dx = \lim_{L \rightarrow \infty} \frac{1}{L} \int_{-L/2}^{L/2} p^*(\tau) e^{+2\pi i \tau u} \int_{-\infty}^{\infty} p(x+\tau) e^{-2\pi i x u} dx [e^{-2\pi i \tau u}] d\tau \\ &= \lim_{L \rightarrow \infty} \frac{1}{L} \int_{-L/2}^{L/2} p^*(\tau) e^{+2\pi i \tau u} \int_{-\infty}^{\infty} p(\sigma) e^{-2\pi i \sigma u} d\sigma d\tau = \lim_{L \rightarrow \infty} \frac{1}{L} \int_{-L/2}^{L/2} p^*(\tau) e^{+2\pi i \tau u} d\tau P(u). \end{aligned} \quad (2)$$



Inspection of Eqs. (1) and (2) shows that

$$S(u) \equiv \text{FT}\{C(x)\} = \lim_{L \rightarrow \infty} \frac{1}{L} |P(u)|^2. \quad (3)$$

Thus, the NPS may be calculated either from the Fourier transform of the autocorrelation function (the indirect method), or from the square of the modulus of the Fourier transform of the data itself (the direct method). Note that since the data  $p(x)$  are real, that  $P(-u) = P^*(u)$ . That is, the NPS at a given negative frequency is equal in magnitude to the NPS at the corresponding positive frequency. Extending the expression of Eq. (3) to two dimensions:

$$S(u,v) = \text{FT}\{C(x,y)\} = \lim_{X,Y \rightarrow \infty} \frac{1}{XY} |P(u,v)|^2. \quad (4)$$

With the advent of the fast Fourier transform (FFT) and fast computers, indirect calculation of the NPS via the autocorrelation function has largely been replaced by the direct method. This paper will discuss only the latter method.

If the stationary random process being characterized by the NPS is also ergodic, as is typically the case for radiographic image noise, then the spectral estimate is found by ensemble averaging. That is, the final NPS is the average of spectra obtained from a series of uniform irradiation images. Then, Eq. (4) becomes

$$S(u,v) = \lim_{X,Y \rightarrow \infty} \left\langle \frac{1}{XY} \left| \int_{-X/2}^{X/2} \int_{-Y/2}^{Y/2} p(x,y) \times e^{-2\pi i(ux+vy)} dx dy \right|^2 \right\rangle, \quad (5)$$

where the pointed brackets denote ensemble averaging.

## B. One-dimensional NPS

The detective quantum efficiency (DQE) is perhaps the best single descriptor of radiographic detector performance. It quantifies how well the detector is able to transfer the signal-to-noise ratio (SNR) inherent in the x-ray fluence at its input to the resulting image. For most two-dimensional (2D) digital imaging detectors, the DQE is a function of at least three independent variables: its two spatial coordinates, and the x-ray exposure. It is a function of a single spatial coordinate for the special case of detectors with an isoplanatic response. The DQE can be written:

$$\text{DQE}(u,v,\varphi) = \frac{(\varphi g)^2 C(u,v) \text{MTF}^2(u,v)}{S(u,v,\varphi) \text{SNR}_{\text{in}}^2}, \quad (6)$$

where  $\varphi$  represents the magnitude of the input x-ray fluence at the detector surface;  $g$  relates changes in the zero-frequency output signal to that at the input (i.e., it is the system gain);  $C(u,v)$  is the Fourier decomposition of the input signal, normalized to unity at maximum amplitude;  $\text{MTF}(u,v)$  is the detector modulation transfer function; and  $S(u,v,\varphi)$  is the output noise power spectrum.<sup>9</sup> Although  $S(u,v,\varphi)$  is a function of the input fluence  $\varphi$ , for notational simplicity it will be referred to hereafter simply as  $S(u,v)$ .

For a monochromatic input x-ray spectrum, or in the case of a photon-counting x-ray detector,  $\text{SNR}_{\text{in}}$  is given by the magnitude of the input fluence  $\varphi$ .

In part because illustration of  $\text{DQE}(u,v,\varphi)$  requires a four-dimensional medium, DQEs of 2D imaging systems are typically presented one spatial frequency coordinate at a time for clarity. By definition,

$$\text{MTF}(u,v) = |\text{2D FT}\{\text{psf}(x,y)\}|, \quad (7)$$

where  $\text{psf}(x,y)$  is the spatial response of the detector to a point x-ray input, or point spread function, and 2D FT represents a two-dimensional Fourier transform. The 1D MTF is typically measured using a narrow slit or edge,<sup>10</sup> and is

$$\text{MTF}(u) = \text{FT}\{\text{lsf}(x)\} = \text{FT}\left\{\frac{d}{dx}[\text{esf}(x)]\right\}, \quad (8)$$

where  $\text{lsf}(x) = \int_{-\infty}^{\infty} \text{psf}(x,y) dy$  is the line spread function and  $\text{esf}(x)$  is the edge spread function. Then,

$$\begin{aligned} \int_{-\infty}^{\infty} \text{lsf}(x) e^{-2\pi i x u} dx &= \left| \int_{-\infty}^{\infty} \{\text{psf}(x,y) dy\} e^{-2\pi i x u} dx \right| \\ &= |\text{2D FT}\{\text{psf}(x,y)\}|_{v=0} \\ &= \text{MTF}(u,0). \end{aligned} \quad (9)$$

Equations (8) and (9) indicate that evaluation of  $\text{FT}\{\text{lsf}(x)\}$  yields  $\text{MTF}(u,0)$ , and thus *the appropriate expression of the NPS for calculation of the single coordinate DQE is  $S(u,0)$* . Similar arguments pertain to  $\text{MTF}(y)$ .<sup>11</sup>

Up to now, most characterizations of  $S(u,0)$  [or  $S(0,v)$ ] of digital radiographic systems have been made using the synthesized slit method.<sup>12-15</sup> In the original development of the method in the analog (film-based) context, the optical aperture of the microdensitometer used to measure the film optical density formed the slit. The methodology has since been applied to digital systems by forming an effective slit from rectangular groups of contiguous pixels. In either case, a long, narrow slit is scanned in steps in one direction over the image. At each step the average intensity in the slit (average transmitted light for a scanning microdensitometer, or average pixel value for a digital system), is recorded. In this way, a one-dimensional data series is generated. The squared modulus of the Fourier transform of the series, after scaling, gives the measured 1D NPS. In the limit of an infinitely long 1D data series in the  $x$  direction, the resulting NPS is<sup>16,17</sup>

$$S_{\text{SS}}(u) = \int_{-\infty}^{\infty} S(u,v) |T(u,v)|^2 dv, \quad (10)$$

where  $T(u,v)$  is the optical transfer function (OTF) of the slit, and where  $S_{\text{SS}}(u)$  is the 1D NPS measured via the scanned slit method. If the slit is rectangular, with  $x$ -dimension  $w$  and  $y$ -dimension  $L$ , then its point spread function is

$$h(x,y) = \left( \frac{1}{w} \text{rect} \frac{x}{w} \right) \left( \frac{1}{L} \text{rect} \frac{y}{L} \right), \quad (11)$$

and therefore,  $T(u,v)$  is



$$T(u, v) = \text{FT}\{h(x, y)\} = \text{sinc}(wu) \text{sinc}(Lv), \quad (12)$$

where the sinc function is defined as

$$\text{sinc}(x) = \frac{\sin \pi x}{\pi x}. \quad (13)$$

Equation (10) becomes

$$S_{SS}(u) = \text{sinc}^2(wu) \int_{-\infty}^{\infty} S(u, v) \text{sinc}^2(Lv) dv. \quad (14)$$

if the slit width is chosen sufficiently narrow, then  $\text{sinc}(wu) \sim 1$  within the range of  $u$  over which  $S_{SS}(u)$  is to be evaluated. In any case, correction of the measured NPS by this factor is straightforward. In a digital system, a synthesized slit of  $1 \times N_L$  pixels constitutes sampling the presampling NPS (the NPS smoothed by the nonzero pixel aperture, but prior to sampling at discrete intervals given by the pixel spacing), using a line of  $N_L$  delta functions, at an interval in the scan direction equal to the center-to-center pixel spacing,  $\Delta x$ . The  $N_L$  sampled values are then averaged. Thus,  $\text{sinc}(wu) \rightarrow \text{sinc}(0) = 1$ , and  $L = N_L \Delta y$ , where  $\Delta y$  is the pixel size perpendicular to the scan direction.

As  $L \rightarrow \infty$ ,  $\text{sinc}^2(Lv)$  becomes sufficiently narrow that  $S(u, v)$  is approximately constant over the range of  $v$  (near  $v = 0$ ) in which  $\text{sinc}^2(Lv)$  is appreciably nonzero, and

$$\begin{aligned} S_{SS}(u) &= \int_{-\infty}^{\infty} S(u, v) \text{sinc}^2(Lv) dv \\ &\approx S(u, 0) \int_{-\infty}^{\infty} \text{sinc}^2(Lv) dv = \frac{S(u, 0)}{L}. \end{aligned} \quad (15)$$

Thus, the desired NPS is  $S(u, 0) = LS_{SS}(u)$ .

Substantial effort has been devoted to understanding the criteria for "sufficiently large  $L$ ." Sandrik and Wagner studied the effect of varying slit length on the 1D NPS of radiographic screen-film systems.<sup>18</sup> They found that the magnitude of the low-frequency NPS is underestimated if the slit length is insufficient, but that the low-frequency components approach a limiting value as the slit length is increased. The slit length required for low-frequency NPS values within 5% of the plateau value was dependent on the particular screen-film combination, but ranged between a value equal to the length of the scan and one nearly twice as long. Koedooder, Strackee, and Venema developed an expression to numerically approximate the integral in Eq. (14).<sup>19</sup> The technique is applicable only to systems with rotational symmetry.

An alternate to the scanned slit approach is to extract a slice along one of the primary spatial frequency axes from the 2D NPS. However, because these slices contain noise power from the orthogonal dimension near to and at zero frequency, low-frequency trends in the data can contribute a significant portion of the noise power unless these trends are first removed. For this reason, the limited number of studies employing this approach have used "thick" slices made by extracting NPS data near to, but not directly on, the primary axes.<sup>20,21</sup> As will be demonstrated below, in some digital detectors this approach can overlook structures that occur

only at zero frequency in the orthogonal dimension (i.e., they are constant in the orthogonal spatial direction, such as a stripe or band).

### C. Digital noise power spectrum

In the above expressions, the 1D and 2D NPS are written as functions of a continuous variable  $p(x)$  that describes the point-to-point fluctuations in the image. In a digital system, this continuous function of the spatial coordinates is sampled at regular intervals,  $\Delta x$ . Thus,  $p(x)$  is evaluated at a set of discrete locations,  $x = n\Delta x$ ,  $n = 0, 1, 2, \dots, N$ , where  $X = N\Delta x$ . Correspondingly, functions of the spatial frequency variable  $u$  are now evaluated at discrete frequencies given by  $u = k\Delta u$ ,  $k = 0, \pm 1, \pm 2, \dots$ . The maximum spatial frequency sampled, the Nyquist frequency, is  $u_N = 1/(2\Delta x)$ . To experimentally estimate the digital NPS, the above continuous expressions must be rewritten in terms of discrete variables. With the preceding definitions, Eq. (3) can be written

$$\begin{aligned} S_d(u) &= S(k\Delta u) \\ &= \lim_{N\Delta x \rightarrow \infty} \frac{1}{N\Delta x} \left| \Delta x \sum_{n=0}^{N-1} p(n\Delta x) e^{-2\pi i(k\Delta u)(n\Delta x)} \right|^2 \\ &= \lim_{N\Delta x \rightarrow \infty} \frac{\Delta x}{N} \left| \sum_{n=0}^{N-1} p(n\Delta x) e^{-2\pi i(k\Delta u)(n\Delta x)} \right|^2, \end{aligned} \quad (16)$$

where  $N$  is the number of samples in the interval  $X$  and the variable  $u$  now takes on the discrete values  $0, \pm 1/X, \pm 2/X, \dots$ . Similarly, Eq. (4) for the 2D NPS becomes

$$\begin{aligned} S_d(u, v) &= S(j\Delta u, k\Delta v) \\ &= \lim_{\substack{N\Delta x \rightarrow \infty \\ M\Delta y \rightarrow \infty}} \frac{\Delta x}{N} \frac{\Delta y}{M} \left| \sum_{n=0}^{N-1} \sum_{m=0}^{M-1} p(n\Delta x, m\Delta y) \right. \\ &\quad \times \left. e^{-2\pi i[(j\Delta u)(n\Delta x) + (k\Delta v)(m\Delta y)]} \right|^2. \end{aligned} \quad (17)$$

The experimentally determined estimate of the digital NPS differs from the underlying analog spectrum in the following ways:

(a) The noise has been convolved with the rect (boxcar) function given by the pixel aperture (deterministic blurring).

(b) The noise data has been sampled at discrete intervals given by the pixel center-to-center spacing (equivalent to multiplication by a Comb function).

(c) The record (image data) used to compute the estimate has been truncated from its original infinite length to a length given in each dimension by the number of points times the sampling interval (equivalent to multiplication by a 2D boxcar function of dimensions  $N\Delta x \times M\Delta y$ ).

The result of (a) is the multiplication of the analog NPS with the absolute square of the 2D sinc function that is the Fourier transform of the pixel aperture function. The result is often referred to as the *presampling* NPS:

$$S_{\text{pre}}(u, v) = S(u, v) |ab \text{sinc}(au) \text{sinc}(bv)|, \quad (18)$$



where  $S(u, v)$  is the analog NPS, and  $a$  and  $b$  are the pixel aperture dimensions.

The result of (b) is that the presampling NPS is convolved with the transform of the sampling Comb function,  $\text{III}(u, v; (1/\Delta x)(1/\Delta y))$ :

$$S_d(u, v) = S_{\text{pre}}(u, v) \otimes \text{III}\left(u, v; \frac{1}{\Delta x} \frac{1}{\Delta y}\right), \quad (19)$$

where  $\Delta x$  and  $\Delta y$  are the sampling intervals in the  $x$  and  $y$  dimensions, and  $\otimes$  denotes two-dimensional convolution. Note that this Comb function consists of an infinite array of delta functions separated in each dimension in frequency space by two times the respective Nyquist frequencies;  $U_N = 1/(2\Delta x)$ ,  $v_N = 1/(2\Delta y)$ .  $S_d(u, v)$  is, therefore, an infinite 2D array of replications of  $S_{\text{pre}}(u, v)$ , with the origin of each  $S_{\text{pre}}$  separated by  $2u_N$  in the  $u$  direction and  $2v_N$  in the  $v$  direction. This replication means that noise beyond the Nyquist frequency overlaps noise below the Nyquist frequency of adjacent replications. This overlap, or *aliasing*, becomes increasingly severe as the spatial sampling interval is increased, that is, as  $S_{\text{pre}}$  is increasingly undersampled. The presampling NPS cannot be directly measured using fine sampling techniques such as those commonly employed to measure the presampling MTF, because the phases of the Fourier components of the image noise are random.<sup>22</sup>

Using digitized screen-film images, Giger, Doi, and Metz have studied the effects on the digital NPS of the sizes of the integrating pixel aperture and the sampling interval.<sup>23</sup> Their results show that aliasing of high-frequency noise (due, for example, to the high-frequency components of x-ray quantum noise) above the Nyquist frequency can form a significant component of the measured digital NPS. Large integrating aperture size (i.e., larger than the sampling interval) tends to reduce the effect of this aliasing by smoothing the high-frequency x-ray quantum noise, at the expense of spatial resolution. Aperture sizes less than the sampling distance increase the overall noise level, and particularly so at high frequencies. Dobbins has recently discussed the impact of undersampling on the interpretation of the MTF of digital systems.<sup>3</sup>

The result of (c) is that the NPS is also convolved with the square of the transform of the data window  $w(x, y)$ :

$$S_{d,w}(u, v) = S_d(u, v) \otimes |W(u, v)|^2, \quad (20)$$

where  $S_d(u, v)$  is the measured NPS, and the frequency window,  $W(u, v)$  is the Fourier transform of the data window  $w(x, y)$ .<sup>24</sup>

If the data series is simply truncated after  $N \times M$  points, corresponding to multiplication of the infinite data sequence by a unity height box of dimensions  $N\Delta x \times M\Delta y$ , then the NPS is convolved with a frequency window with modulus

$$|W(u, v)| = N\Delta x M\Delta y \frac{\sin(\pi N\Delta x u) \sin(\pi M\Delta y v)}{\pi^2 N\Delta x u M\Delta y v}. \quad (21)$$

A variety of data windows have been studied in many signal processing contexts, with the optimum choice for a

given situation depending on the characteristics of the particular spectrum being characterized. Selection of a data window is based on the shape and width of the resulting frequency window. In general, there is a compromise between the width of the central lobe and the magnitude and extent of any side lobes. A broad central lobe reduces spectral resolution, and significant side lobes produce *leakage*, wherein noise power from nearby frequencies are mixed in the convolution process. In the case of power spectra exhibiting strong periodic components, as is the case in many digital radiographic systems, minimization of side lobe magnitude is often necessary for distinguishing small amplitude features adjacent to large amplitude peaks.<sup>25,26</sup>

## D. Experimental estimation of the noise power spectrum

### 1. Uncertainty in the spectral estimates

Because noise in a radiographic image arises from stochastic (random) processes, any realization (image) of the noise associated with those processes is merely a sample chosen from the ensemble of all possible samples. Thus, there is an inherent statistical uncertainty in the representation of the underlying (true) population variance by that sample. In this regard, Fourier decomposition of image noise (such as is performed in determination of the NPS) is different from the decomposition of signal (such as is performed in determination of the modulation transfer function), where amplitudes and phases are known and fixed. The variance in the spectral components of the measured NPS is independent of the number of data points (e.g., the number of pixels) in the sample used to calculate it, and for mean-zero, normally distributed noise, results in a coefficient of variation (COV) of approximately unity for each spectral estimate,  $S(u, v)$  except at zero frequency and the Nyquist frequency, where the COV is  $2^{1/2}$ .<sup>27</sup> The variance (uncertainty) in the estimate can be reduced by sectioning the entire  $N\Delta x \times M\Delta y$  noise record into a number of contiguous blocks, and averaging the spectra obtained from each (ensemble averaging). The COV of the final estimate decreases as the inverse square root of the number of determinations. However, the spectral *resolution* is inversely proportional to the number of data points used to generate each NPS. Thus, for a fixed amount of data, there is a tradeoff between frequency resolution and variance in the final NPS estimate. For example, if  $N$  data points, spaced at an interval  $\Delta x$ , are used to calculate a 1D NPS, then the spectral resolution and COV are, respectively,<sup>27</sup>

$$\Delta f = \frac{1}{N\Delta x}, \quad \text{COV} \cong 1.0. \quad (22)$$

If these  $N$  points are divided into  $n$  successive sections, then the frequency resolution and COV become

$$\Delta f = \frac{1}{\left(\frac{N}{n}\right)\Delta x} = \frac{n}{N\Delta x}, \quad \text{COV} \cong \frac{1.0}{\sqrt{n}}. \quad (23)$$



TABLE I. Summary of the various components of the NPS and methods for isolating each. The NPS components are (a) random (stochastic), (b) nonstochastic but varying from one image to another, and (c) nonstochastic and fixed from image to image (fixed pattern noise).

NPS	Method	Components present
$S_{\text{tot}}(u,v)$	Average spectra from individual images	Stochastic, varying nonstochastic, fixed pattern
$S_{\text{diff}}(u,v)$	Average 0.5 times spectra from difference images	Stochastic, varying nonstochastic
$S_{\text{avg}}(u,v)$	Spectrum from average of many images	Varying nonstochastic, fixed pattern
$S_{\text{f.p.}}(u,v)$	$S_{\text{tot}}(u,v) - S_{\text{diff}}(u,v)$	Fixed pattern
$S_{\text{v.n.}}(u,v)$	$S_{\text{avg}}(u,v) - S_{\text{f.p.}}(u,v)$	Varying nonstochastic
$S_{\text{stoch}}(u,v)$	$S_{\text{tot}}(u,v) - S_{\text{avg}}(u,v)$	Stochastic

## 2. Stochastic and nonstochastic components

Image noise can be categorized as (a) random (stochastic), (b) nonstochastic but varying from one image to another, or (c) nonstochastic and fixed from image to image (fixed pattern noise). For a complete description of image noise, each component should be analyzed.

Fixed pattern noise usually arises from spatial variations in detector sensitivity. Although theoretically fixed pattern noise should be removed during routine postacquisition image processing (flat fielding), the removal may be incomplete or its completeness may be signal dependent. Note that since flat fielding typically involves division of the raw image by a normalized, highly averaged raw flood image, random noise in areas of low gain (average output signal per incident x ray) is amplified in the flat fielding process, while that in areas of high gain is reduced. Nonstochastic noise that is present intermittently or varies in location from image to image will not be reliably removed during flat fielding. An example of this type of noise is 60 Hz power line pickup during detector readout.

The NPS obtained by averaging the spectra of many single uniform irradiation images,  $S_{\text{tot}}(u,v)$ , contains components from all three types of noise. The NPS using the difference of two images obtained under identical conditions of uniform irradiation (and divided by 2),  $S_{\text{diff}}(u,v)$ , contains variance from stochastic and varying nonstochastic components, but none from fixed pattern noise. The magnitude of the noise power from fixed pattern noise can be determined from  $S_{\text{f.p.}}(u,v) = S_{\text{tot}}(u,v) - S_{\text{diff}}(u,v)$ . Note that the NPS obtained from a highly averaged image,  $S_{\text{avg}}(u,v)$ , differs from  $S_{\text{f.p.}}(u,v)$  by an amount equal to the noise power due to any time-varying nonstochastic components. The stochastic NPS components can be found by subtracting  $S_{\text{avg}}(u,v)$  from  $S_{\text{tot}}(u,v)$ .<sup>28</sup> Table I summarizes the methods for isolating spectral components due to these three types of noise.

## III. METHODS

### A. Data acquisition

Both mammographic systems evaluated utilize molybdenum target x-ray tubes, with molybdenum or rhodium filtra-

tion. Data were acquired using Mo/Mo spectra and a variety of kVp and mAs settings. A block of acrylic 3.8 cm thick and sufficiently large to cover the entire detector surface was placed on the breast support to create realistic spectral composition and scatter conditions. In selecting areas of the image for estimating noise power spectra, care was taken to avoid regions near the image periphery, where the scatter contribution is nonuniform. Detector entrance exposures were calculated by raising the acrylic block slightly above the detector surface, and using a thin ion chamber to measure the exposure at its exit surface. Corrections were then applied to account for the slight difference between the location of the chamber and the detector entrance surface, relative to the focal spot. For each selected kVp and mAs, eight images were obtained. Data used for spectral estimates were taken from  $\sim 5 \text{ cm} \times 5 \text{ cm}$  regions, located centrally in the image. The data regions were divided into the maximum number of contiguous sections consistent with the NPS estimation technique to be used (e.g.,  $N \times L$  pixel sections for a scan in the  $x$  direction, or  $N \times M$  pixels for a 2D NPS calculation). Spectra were calculated from each section of each of the eight images, and were then averaged. The final ensemble-averaged NPS estimates were thus averages of  $\sim 300$ – $1200$  spectra, resulting in standard errors of  $\sim 3\%$ – $6\%$ .

### B. Subtraction of background trends

Low-frequency background trends, such as those from the x-ray source heel effect, are often present in the data. Although such trends may have significant Fourier components only at frequencies below the lowest measurable frequency in the power spectrum ( $1/N\Delta x$ ), leakage into low-frequency spectral components can artificially inflate the low-frequency NPS. (As discussed in Sec. II C, leakage is the spreading of spectral power from one frequency to adjacent frequencies, and is a result of the nonzero width of the frequency window, which is the Fourier transform of the finite data window.) For this reason, noise power spectra are frequently obtained by first subtracting one uniform exposure image from another made with the same exposure, and dividing the NPS, resulting from the subtracted image, by 2. The factor of



2 accounts for the fact that the variance in the subtracted image gets approximately equal contributions from the uncorrelated noise in the two original images. Alternately, a difference image may be obtained by subtracting a highly averaged uniform exposure image from a single image. The random noise in the highly averaged image is negligible if a large number of images is used to obtain it.

The image subtraction technique has the drawback, however, of also removing any uncorrected fixed pattern noise occurring at higher frequencies. Thus, this method may not be optimum for estimating the NPS of clinical images following uniformity correction (flat fielding), because noise removed in the subtraction process would nevertheless be present in clinical images. We have, therefore, evaluated two methods for removing low-frequency background trends from single images: subtraction of a low-pass-filtered version of the image, and subtraction of a low-order polynomial fit to the image. When using the first method, for simplicity, a rectangular (boxcar) filter was used to filter the entire 2D data set. Subtraction of the resulting filtered image from the original is equivalent to subtraction of a running local means as has been employed for one-dimensional data by others.<sup>23</sup> Convolution in coordinate space with a rectangular filter is equivalent to multiplication in frequency space by a sinc function. The dimensions of the square filtration kernel were chosen sufficiently large that the first zero crossing of the resulting sinc function was at or below the minimum frequency sampled in the NPS. In the second method of background trend subtraction, a two-dimensional polynomial was first fit to each uniform exposure image, and subtracted. Both first- and second-degree polynomials were evaluated.

In order to compare the above two methods of background trend subtraction, a synthetic data set was created. The data consist of a dc (average) pixel value, a normally distributed random component, a periodic component (one in each dimension), a linear (ramp) component, and a second-order component. The digital value  $p(i,j)$  of the pixel in the  $i$ th column and  $j$ th row was computed as

$$p(i,j) = d_1^*[\text{rand}(i,j)] + d_2(i,j), \quad (24)$$

where the  $\text{rand}()$  operator generates one of a set of normally distributed random numbers with average zero and standard deviation one,  $d_1$  is a scaling factor, and

$$d_2(i,j) = a_0 \sin(iu_p + \delta_u) + b_0 \sin(jv_p + \delta_v) + a_1 i + b_1 j + a_2 i^2 + b_2 j^2 + C_0, \quad (25)$$

where  $u_p$  and  $v_p$  are the spatial frequencies of the periodic components in the  $x$  and  $y$  directions, respectively, and  $\delta_u$  and  $\delta_v$  are phase factors. The constant  $C_0$  sets the magnitude of the dc component, and the constants  $a_0$ ,  $b_0$ ,  $a_1$ ,  $b_1$ ,  $a_2$ , and  $b_2$  set the magnitudes of the periodic, linear, and quadratic components in the  $x$  and  $y$  directions, respectively. Figure 1 is a gray-scale plot of a portion of one of the synthetic data sets.

Figure 2 shows a semilog plot of four representative 1D power spectra generated from synthetic data. The spectrum labeled with diamonds is that of a data set with no back-

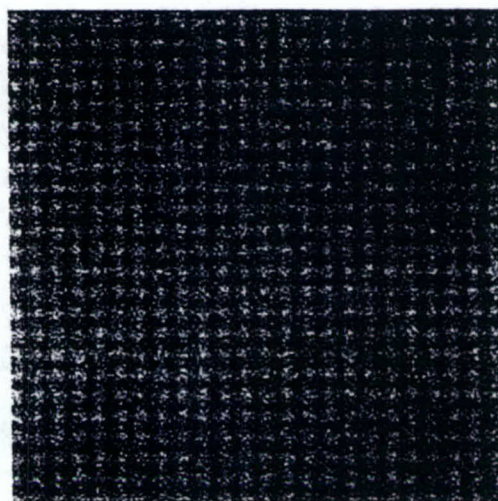


FIG. 1. Gray-scale image of a synthetic data set used to evaluate methods of background trend removal. For ease of visualization, the data set shown contains only sinusoidal, random, and dc components (no linear or quadratic component).

ground trend ( $a_1 = a_2 = b_1 = b_2 = 0$ ). The second spectrum, labeled with squares, is from the same data, but with linear and quadratic components added. The third and fourth spectra (triangles and crosses), are calculated following trend removal via subtraction of a least-squares surface fit to a second-order polynomial or by subtraction of a boxcar-filtered version of the image, respectively. In this example, the boxcar filter was  $64 \times 64$  pixels, the same size as the sections of data used to calculate the 2D NPS. The spectrum obtained with no trend removal demonstrates substantial leakage of low-frequency noise power into the frequency range of the periodic component. Figure 2 shows that both trend removal techniques reduce the low-frequency noise power sufficiently that it is no longer apparent in the spectrum, even though the leakage is unchanged. The quadratic fit technique virtually restores the original NPS, a result not surprising given the quadratic nature of the trend.

Figure 3 also shows the effects of different trend removal techniques, this time using flat-field image data obtained from one of the mammography detectors. The 2D spectra were computed from the average of 648  $128 \times 128$  pixel sections. Thin slices were extracted along the  $v$  axis. Again, slices are shown from 2D spectra following no trend removal, and following subtraction of either a fitted quadratic surface or a low-pass-filtered data set. In addition, two different size convolution kernels for low-pass filtering are compared. For a rectangular,  $n \times m$  pixel convolution kernel of amplitude  $(n\Delta x m\Delta y)^{-1}$ , where  $\Delta x$  and  $\Delta y$  are the pixel size in the  $x$  and  $y$  dimensions, the trend-corrected NPS is given by

$$S_{d,w,b} = S_{d,w} [1 - \text{sinc}(n\Delta x u) \text{sinc}(m\Delta y v)]. \quad (26)$$

In order that only noise power close to dc is removed, one would like the term  $\text{sinc}(n\Delta x u) \text{sinc}(m\Delta y v)$  to be appreciable only for very low frequency. Therefore, the quantities



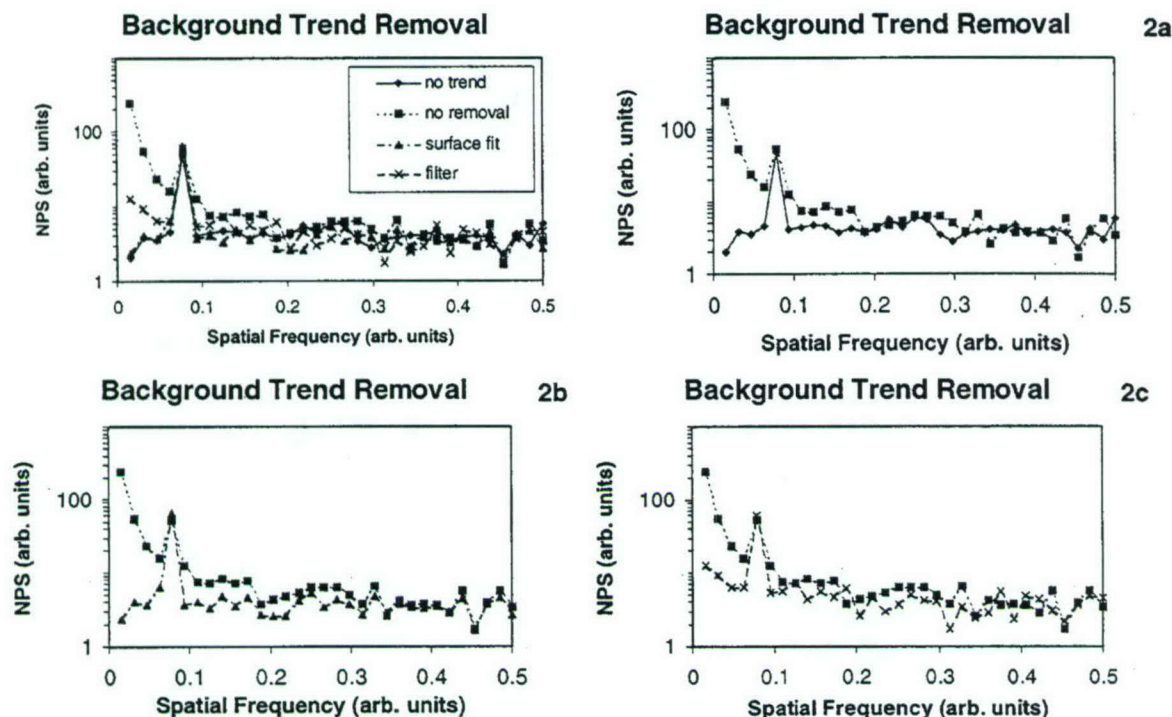


FIG. 2. Comparison of background trend removal techniques, using a synthesized data set. (a) shows the NPS calculated from data with no background trend (diamonds), and the same data but with linear and quadratic trends added (squares). (b) compares the data with linear and quadratic trends added before (squares) and after subtraction of a two-dimensional second-order polynomial fit to the data (triangles). (c) compares the data with linear and quadratic trends added before (squares) and after subtraction of a low-pass-filtered version of the data (crosses).

$n\Delta x$  and  $m\Delta y$ , corresponding to the reciprocal of the first zero crossings of the sinc functions in the two dimensions, must be sufficiently large compared to the lowest frequency of interest in the NPS. In Fig. 3,  $S_{d,w,b}$  is shown for  $n=m=100$  and for  $n=m=200$ . Note that for  $m=100$ , the first zero crossing of  $\text{sinc}(m\Delta yv)$  is at a slightly higher frequency than the lowest frequency ( $v=1/(128\Delta y)$ ) in the spectrum. The effect is a slight reduction in the noise power at the lowest frequency, relative to that shown for  $m=200$ . Because of this, in general, we have found the best results by making the size of the smoothing kernel somewhat larger than the size of the blocks used to calculate the individual 2D spectra.

It should be noted that 2D quadratic fitting carries a significantly higher cost in processing time than does 2D smoothing. This is true even if the fits are performed on the relatively smaller blocks individually, rather than on the full data set. For example, on a Sun Sparcstation 10 in our laboratory, trend removal using 2D fits to 800  $128 \times 128$  blocks takes approximately 4 h of processing time, whereas only a few minutes are required for 2D smoothing of the same amount of data.

### C. Units and scaling

The noise power spectrum is more precisely termed the power spectral density, that is, the noise power per unit frequency.<sup>8</sup> The quantity  $S(u,v)dudv$  is the contribution to the variance from noise components with spatial frequencies between  $u$  and  $u+du$ , and  $v$  and  $v+dv$ .  $S(u,v)$  thus has

dimensions of inverse spatial frequency squared. The correct scaling of the NPS can be verified by observing that the volume (area) under the 2D (1D) NPS equals the total variance. Thus, integration over frequency of spectra estimated using mean-zero sections from uniform illumination images

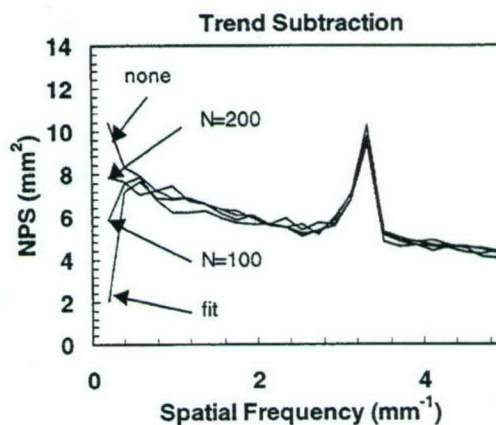


FIG. 3. Comparison of background trend removal techniques, applied to images obtained with one of the digital mammography systems, obtained using nominally uniform irradiation. The graph shows four 1D power spectra,  $S(0,v)$ , obtained from thin cuts from four different 2D spectra. The 2D spectra were calculated following (a) no trend removal (none), (b) subtraction of a fitted quadratic surface (fit), (c) subtraction of a low-pass-filtered version of the data using a  $100 \times 100$  pixel convolution filter, and (d) same as (c), but using a  $200 \times 200$  pixel filter.



should numerically equal the mean-square deviations from their average of the pixel values in those sections.

Noise power spectra are sometimes presented normalized by the square of the large-area (average) output signal.<sup>20,21</sup> This normalization has the effect of compensating for difference in gain between two systems which are being compared, and of simplifying the expression for the DQE. With this normalization, Eq. (6) becomes

$$\text{DEQ}(u,v,\varphi) = \frac{C(u,v)\text{MTF}^2(u,v)}{\tilde{S}(u,v,\varphi)\text{SNR}_{\text{in}}^2} = \frac{C(u,v)}{\text{SNR}_{\text{in}}^2} \text{NEQ}(u,v,\varphi), \quad (27)$$

where  $\tilde{S}(u,v,\varphi) = S(u,v,\varphi)/(\varphi g)^2$  is the normalized NPS, and  $\text{NEQ}(u,v,\varphi)$  is the noise equivalent quanta.

## IV. RESULTS

### A. Two-dimensional NPS

Neglecting digitization noise, the additive noise in the NPS obtained from a CCD-based digital mammography detector can be written as

$$\sigma_a^2 = \sigma_t^2 + \sigma_r^2 + S_p(u,v), \quad (28)$$

where  $\sigma_t$  is the CCD thermal (Johnson) noise,  $\sigma_r$  is the read noise, and  $S_p(u,v)$  is the variance due to frequency-dependent periodic noise. These noise contributions are summed in quadrature because they are independent with respect to each other. Periodic noise can arise from capacitively coupled clock pulses, electromagnetic interference from power supplies, or 60 Hz pickup due to ground loops. The location in the image of the noise due to such periodic interference is not fixed from frame to frame, because its phase (in time) is not fixed with respect to detector readout. It is, therefore, not removed during the uniform correction. Note that spikes from periodic additive noise are apparent on the  $v$  axis (the central, vertical axis in each of the plots in Fig. 4), but not on the  $u$  axis. As is shown below, these same structures are apparent in the 1d spectra obtained by scanning a synthetic slit in the  $y$  direction.

2D spectra obtained from both developmental systems exhibit strong periodic structures over all exposure ranges tested. These structures take the form of sharp peaks in the spectra, and are due to periodic additive noise. Figure 4 shows gray-scale plots of the 2D spectra of one digital mammographic system at four exposure levels. Gridlines are spaced at  $1 \text{ mm}^{-1}$ . With increasing x-ray exposure, the periodic noise peaks are decreasingly apparent as their magnitude becomes progressively less relative to that of the x-ray quantum noise contribution at low frequency.

### B. Effect of varying slit length on 1D NPS

We have studied the effect of varying the length of the synthetic scanning slit used for the estimation of  $S(u,0)$  or  $S(0,v)$ . Figure 5 shows 1D spectra obtained from uniform illumination images using an exposure of 38 mR at the detector surface. Each of the spectra shown in the plot was generated by stepping a synthetic slit with  $x$  and  $y$  dimen-

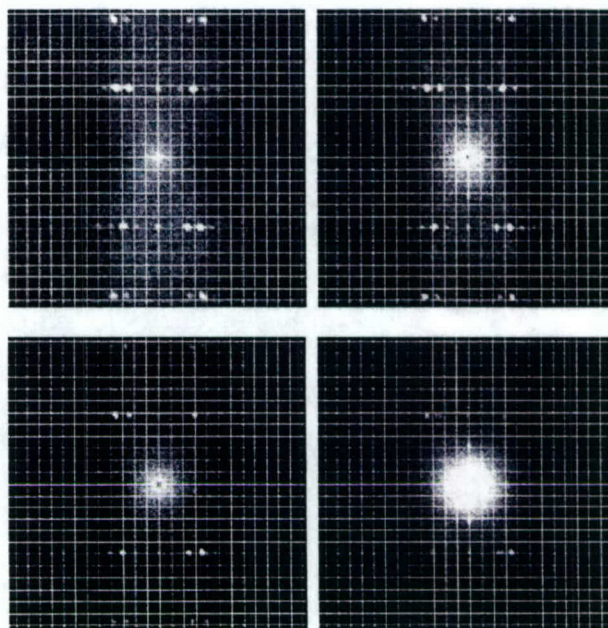


FIG. 4. (a) 2D NPS at 9 mR exposure to the detector surface. Gridlines are spaced by  $1 \text{ mm}^{-1}$ . (b) 2D NPS at 18 mR exposure to the detector surface. Gridlines are spaced by  $1 \text{ mm}^{-1}$ . (c) 2D NPS at 38 mR exposure to the detector surface. Gridlines are spaced by  $1 \text{ mm}^{-1}$ . (d) 2D NPS at 76 mR exposure to the detector surface. Gridlines are spaced by  $1 \text{ mm}^{-1}$ .

sions of  $1 \times L$  pixels, over the data in the  $x$  direction in steps of one pixel. The longest slit length shown ( $L = 512$  pixels) corresponds to a slit approximately 20 mm long. At each step, the pixels in the slit were averaged. The resulting 128 element series was then Fourier transformed and scaled as follows to give the measured 1D NPS. Combining Eqs. (15) and (16) we have

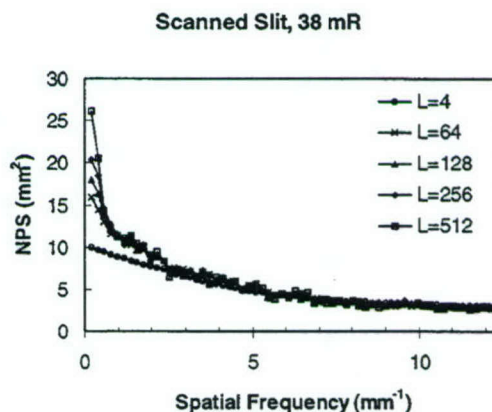


FIG. 5. 1D noise power spectra obtained from the same data set, but with various scanning slit lengths. Spectral components above approximately 0.6 cycles per millimeter are insensitive to changes in slit length for slit lengths of 64 pixels or greater. However, a slit length of 4 pixels results in underestimation of the noise power out to  $\sim 3$  cycles per millimeter.



$$S(k\Delta u) = \lim_{\substack{N\Delta x \rightarrow \infty \\ N_L\Delta y \rightarrow \infty}} N_L\Delta y \frac{\Delta x}{N} \times \left| \sum_{n=0}^{N-1} p'(n\Delta x) e^{-2\pi i(k\Delta u)(n\Delta x)} \right|^2, \quad (29)$$

where  $p'(n\Delta x) \equiv 1/N_L \sum_{l=0}^{N_L-1} p(n\Delta x, l\Delta y)$  is the average of the pixel values in the synthetic slit. Note that from Eq. (17), a section of the digital 2D NPS along the  $u$  axis, calculated from a  $N \times M$  section of the image, is

$$S(k\Delta u, 0) = \lim_{\substack{N\Delta x \rightarrow \infty \\ M\Delta y \rightarrow \infty}} \frac{\Delta x}{N} \frac{\Delta y}{M} \times \left| \sum_{n=0}^{N-1} e^{-2\pi i[(k\Delta u)(n\Delta x)]} \sum_{m=0}^{M-1} p(n\Delta x, m\Delta y) \right|^2. \quad (30)$$

For the special case when the slit length  $N_L\Delta y$  is equal to the scan length  $N\Delta x$ , Eq. (29) and (30) reduce to the same expression:

$$S(k\Delta u, 0) = \lim_{\substack{N\Delta x \rightarrow \infty \\ N_L\Delta y \rightarrow \infty}} \frac{\Delta x}{N} \frac{\Delta y}{N_L} \times \left| \sum_{n=0}^{N-1} e^{-2\pi i[(k\Delta u)(n\Delta x)]} N_L p'(n\Delta x) \right|^2. \quad (31)$$

Thus, for example, a cut along the  $u$  axis from a  $128 \times 128$  2D NPS is identical to the 1D NPS obtained by scanning a  $1 \times 128$  pixel synthetic slit over 128 pixels in the  $x$  direction. In all cases, we verified that the 1D NPS obtained from the scanned slit method with the slit length equal to the size of the data block used to generate the 2D NPS, was identically equal to the section from the 2D spectrum along the  $u$  or  $v$  axis.

As shown in Fig. 5, the very low-frequency values of the 1D NPS did not converge to a plateau value for slit lengths of up to 512 pixels, which is four times the scanned distance. This behavior is similar to that observed by Sandrik and Wagner for the Kodak Hi-Plus/XRP screen-film system.<sup>18</sup> In that study, measured NPS values at 0.39 cycles/mm continued to increase with increasing slit length up to  $L = 5.9$  mm for scan a distance of 2.5 mm, while convergence to a plateau value was observed for other screen-film systems at similar frequencies.

### C. Slices from the 2D NPS

Notably, in the context of the evaluation of storage phosphor systems, 1D spectral estimates have been obtained by extracting thick cuts from the 2D NPS. The cuts are made parallel to the primary axis of interest, but do not include the axis, so as to avoid low-frequency trending effects. We have evaluated this approach for analysis of the spectra of the digital mammography systems. Figure 6 is a plot comparing a thin cut (a single-frequency-bin wide) along the primary

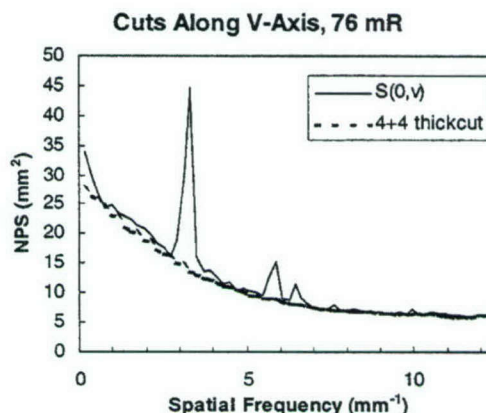


FIG. 6. Slices from 2D NPS of digital mammographic system. The solid line is a slice one-bin wide, along the  $v$  axis. The dotted line is the sum of two four-bin sections taken from either side of the  $v$  axis. Differences between the two occur primarily at low frequency and because of an-axis periodic noise components.

( $v$ ) axis of the 2D NPS with a thick cut generated by summing the two four-bin-wide sections immediately on either side of, and adjacent to, the  $v$  axis. The thick slices adequately represent the on-axis slice except at low frequency, where the NPS decreases rapidly with increasing  $u$ . Of greater significance is the omission of the periodic noise structures near spatial frequencies of 3 and 6 cycles/mm. These represent noise power from fluctuations in the  $y$  direction (left to right direction of the breast support) that are constant in the anterior-chest direction. Such noise may appear as horizontal stripes in the mammographic image.

As would be expected, thicker slices are poorer approximations to the on-axis cuts, as the falloff in the 2D NPS in the dimension orthogonal to the slices causes the average spectral values to be reduced. This produces an effect similar to that resulting from utilization of a scanning slit of insufficient length.

### D. NPS of the developmental mammographic systems

Spectral estimates were obtained from images acquired using two developmental digital mammography systems located at the University of Virginia. Both systems contain butted arrays of CCD-based modules, but they differ in the type of x-ray converter and in the details of the optical coupling to the CCDs. The pixel size is  $\sim 37 \mu\text{m}$  for system 1 and  $\sim 47 \mu\text{m}$  for system 2. The NPS of uniform illumination images from both digital mammographic systems was measured over a range of detector entrance surface exposures from 9 to 78 mR. For each exposure, 2D noise power spectra estimates were made as described in Sec. III A. Figures 7(a) and 7(b) are semilog plots of cuts along the  $u$  and  $v$  axes of both systems at four exposure levels. The spectra have been normalized by the respective large-area output signal squared. Immediately apparent from Fig. 7 is the fact that the noise behavior of system 1 is different in the  $x$  and  $y$  dimensions, with the  $y$  dimension exhibiting significantly greater



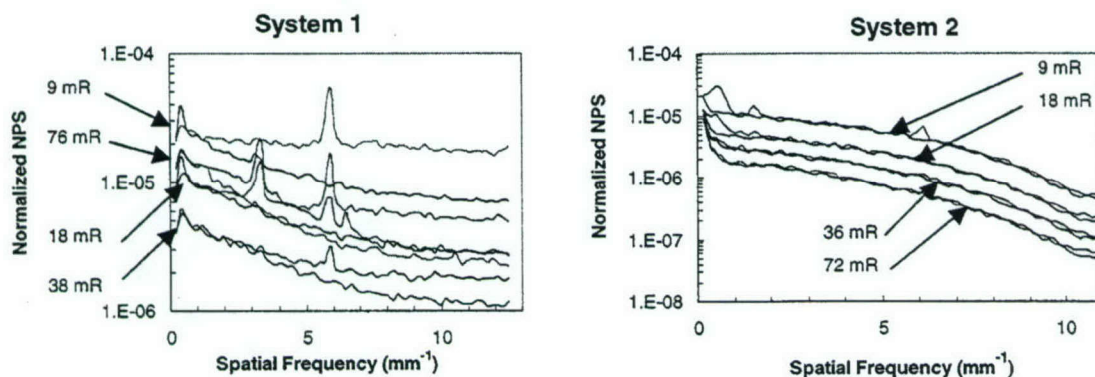


FIG. 7. Noise power spectra of the two developmental digital mammography systems studied. Spectra are shown at four exposures for each system. In the spectra of system 1, the magnitude of  $S(u,v)$  exceeds that of  $S(u,0)$  at high frequency for all exposures, even though their magnitudes at low frequency are equal.

noise at high frequency. In both systems, the  $y$  direction corresponds to the parallel transfer direction of the CCDs. Also, while the magnitude of the system 2 NPS decreases monotonically with increasing exposure, that of system 1 is higher at 76 mR than at 18 or 36 mR. This unexpected increase in noise is caused by the appearance of uncorrected fixed pattern noise in the images of system 1 at higher exposures.

Also apparent are the very different shapes of the spectra obtained from the two systems, with the spectra of system 1 leveling off at high frequency, while those of system 2 continue decreasing out to the Nyquist frequency. At all exposures tested, the normalized noise power of system 2 is less than  $10^{-6}$  at Nyquist. As is shown below, attenuation of the high-frequency noise in system 2 is primarily a result of the smoothing effect of the spatial dewarping algorithm used.

### E. Comparison with pixel variance

Each of the 2D spectra presented in this study was integrated over spatial frequency in order to compare the resulting value with the variance calculated from the pixel-to-pixel fluctuations. The integrals were calculated over the range from  $-f_N$  to  $+f_N$ , where  $f_N$  is the Nyquist frequency. In all cases, differences between the integrals and the directly calculated total variance were less than 0.5%.

Figure 8 shows the total noise of the two digital mammography detectors over the range of exposures from 9 to 78 mR. The noise was determined from the square roots of the integrated volumes under the 2D spectra whose axial slices are shown in Fig. 7. Figure 8 plots the log of the noise versus the log of the exposure. For both systems, straight lines have been fit to the experimentally determined data points, and the calculated slopes of the lines are shown in Fig. 8. In a system for which x-ray quantum noise is the dominant noise source, the slope of such a plot is approximately 0.5. A slope less than 0.5 indicates the presence of significant contributions to the noise power from sources other than x-ray noise.

### F. Effects of image correction

All detectors exhibit imaging characteristics that are imperfect but constant from image to image. This type of imperfection, including the presence of turned-on or dead pixels, local or global spatial distortions, and spatially fluctuating sensitivity, can be corrected in software. However, correction algorithms can have an appreciable effect on the noise power spectra, and care must be taken in this regard when interpreting the spectra. Figure 9 shows two pairs of spectral estimates calculated from the same set of uniform x-ray exposures. In one pair, the raw data (prior to any corrections) were used. In the other case, the data were processed using the sequence of calibration steps typically applied to clinical data: masking of bad pixels, subtraction of a dark frame, geometric dewarping, and sensitivity nonuniformity correction. For both raw and processed data, spectral estimates were calculated from difference images obtained by subtracting one image from another, pixel by pixel. The most apparent difference between the spectra of the raw and calibrated images is at high frequency, where the calibrated

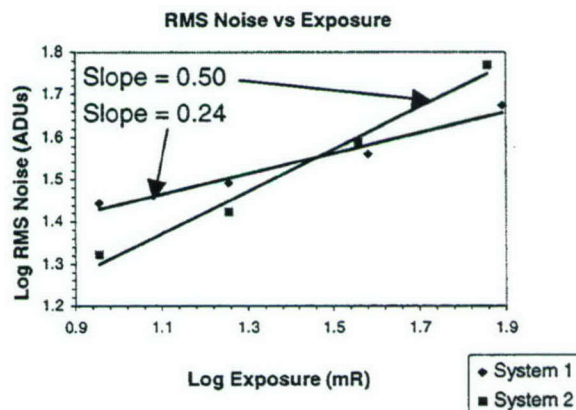


FIG. 8. Log noise vs log exposure for two digital mammographic detectors. The noise was found from the square root of the integrated volume under the 2D NPS. The plot shows the slope of straight lines fit to the measured data.



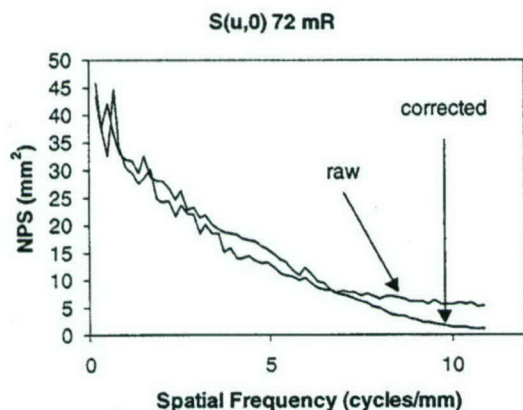


FIG. 9. Comparison of the NPS obtained from corrected vs raw image data. The reduction in the high-frequency noise in the corrected image spectra occurs during dewarping. Of course, the detector MTF exhibits a similar reduction at high frequency.

images exhibit much less noise power. The cause of the attenuation of high-frequency noise is the dewarping algorithm. During dewarping, the signal in the raw image is reassigned to new locations in the dewarped image based on a matrix of displacement vectors stored in a look-up table. In general, a signal from any given pixel in the warped image is mapped to a location that does not coincide with the center of a pixel in the dewarped image. One method of handling this is to perform a proximity-weighted distribution of the signal among pixels whose boundaries fall within a half pixel of the corrected location. This has the effect of smearing out the signal content of each pixel in the raw image over several pixels in the dewarped image, a smoothing operation.

Note that this method of dewarping is only one of many potential approaches, each of which can have a different effect on the final image. An important function of noise power spectral analysis is to identify the impact of various image-correction algorithms on the image noise. For this reason, it is useful to obtain noise power spectral estimates both from corrected data and, when available, from raw data.

### G. Effects of aliasing

Aliasing of noise components present above the Nyquist frequency is unavoidable because the only estimate of the NPS available from a digital system is that obtained following sampling by the digital matrix. In order to estimate the effect of aliasing in the measured NPS of the digital mammographic systems, cascaded linear systems analysis was used to calculate the presampling NPS.<sup>6,29-33</sup> Details of the theoretical development are presented elsewhere.<sup>34</sup> For both systems, the presampling NPS can be written as

$$S_{\text{pre}}(u, v) = \frac{G^2 \Phi_0}{\eta A_s} |MTF(u, v)|^2 + [(G \Phi_0) + \sigma_r^2] \times |\text{sinc}(p_x u) \text{sinc}(p_y v)|^2 + \sigma_r^2, \quad (32)$$

where  $G$  is the system gain in CCD electrons per incident x-ray photon;  $\Phi_0$  is the incident x-ray fluence per pixel;  $\eta$  is

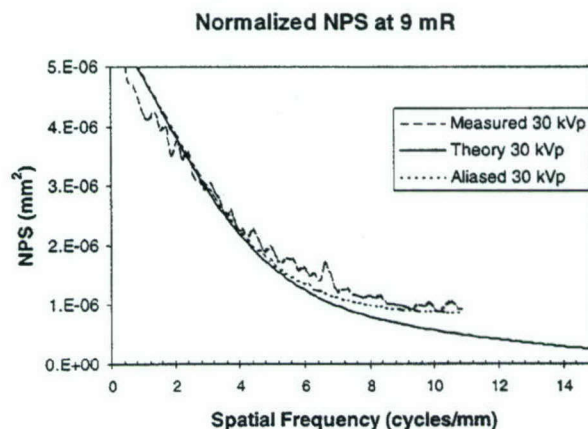


FIG. 10. Comparison of measured and theoretical digital NPS. To calculate the theoretical digital NPS, noise power in the theoretical presampling NPS above the Nyquist frequency was aliased into the frequency range between zero and Nyquist. The presampling NPS was calculated using cascaded linear systems analysis. Although the system gain, phosphor absorption efficiency, and Swank factor are all energy dependent, their spectrally weighted values are approximately:  $G \sim 3.5$  e-/incident x ray,  $\eta \sim 0.50$ , and  $A_s \sim 0.90$ .

the x-ray absorption efficiency;  $A_s$  is the Swank factor;  $MTF(u, v)$  is the overall detector MTF;  $\sigma_1$  is the rms CCD thermal noise in electrons;  $p_x$  and  $p_y$  are the pixel sizes in the  $x$  and  $y$  dimensions, respectively; and  $\sigma_r$  is the rms read noise in electrons.  $G$ ,  $\Phi_0$ ,  $\eta$ , and  $A_s$  are each functions of the x-ray photon energy, and bars above symbols denote weighted averages over the x-ray spectrum incident at the detector surface. Figure 10 shows an example of the aliased noise in images obtained at 9 mR exposure using one of the developmental systems. Plotted are the measured digital 1D spectra,  $S_d(u, 0)$  and  $S_d(0, v)$  obtained from differences of raw images; the calculated presampling spectrum,  $S_{\text{pre}}$ ; and the calculated digital NPS,  $S_{\text{digital}}$ . In calculating the digital NPS,  $S_{\text{pre}}$  values between one and two times the Nyquist frequency were added to those in the interval between 0 and the Nyquist frequency, according to the formula

$$S_{\text{digital}}(\omega) = S_{\text{pre}}(\omega) + S_{\text{pre}}(2\omega_N - \omega) - \sigma_r^2, \quad 0 < \omega \leq \omega_N. \quad (33)$$

The variance due to read noise is not aliased because it is added after the digital sampling process, and is merely an offset in the measured NPS. The calculated noise power above twice the Nyquist frequency is negligible. The close agreement in Fig. 10 between the measured NPS and the calculated NPS with aliasing shows that aliased noise can constitute a significant fraction of the high-frequency noise power in the mammographic systems. Note, however, that dewarping (c.f. Fig. 9) smooths the high-frequency noise, thereby greatly reducing the effects of aliasing.

### V. DISCUSSION

Similarly to other types of radiographic systems, digital detectors for mammography can usefully be characterized through Fourier analysis of their noise characteristics. However, investigators preparing to estimate noise power spectra



of such system are confronted with a bewildering array of procedural considerations, lack of attention to which can lead to misleading results. Limitations formerly imposed by the tradeoff between spectral resolution and uncertainty in the spectral estimates are much less stringent than even a decade ago, since significant digital processing power is now available to the majority of medical physicists. Thus, ensemble averaging over a large number of images obtained using uniform x-ray exposure is feasible, thereby permitting fairly subtle features of the NPS to be resolved. The necessary resolution is determined by the proximity in Fourier space of relevant features and should be determined on a system-by-system basis. For the digital systems characterized in this paper,  $128 \times 128$  2D spectra, yielding 64 frequency bins in the single-sided 1D spectra, were sufficient to resolve the features of interest. Occasionally, we found it useful to recalculate particular spectra at higher resolutions. This may be useful, for example, for assurance that low-frequency structures are, in fact, independent of background trend noise power residing in the lowest-frequency bin (the range between zero and  $1/N\Delta x$ , where  $N\Delta x$  is the length of the data series).

The noise in images from both the digital mammographic systems has markedly nonisoplanatic properties, particularly at low exposure where frequency-dependent system noise is most predominant. Such noise can be due to digital clock pulses that are radiatively or capacitively coupled to the analog data signals. Furthermore, the majority of this noise power resides away from the principle spatial frequency axes, and thus, does not appear on the 1D NPS, whether it is obtained from an extracted slice of the 2D NPS, or from a scanned slit. It is, therefore, important that the full 2D NPS be estimated, even if 1D spectra are subsequently used for SNR calculations.

The scanned slit method for obtaining 1D spectra yielded results identical to those obtained from thin cuts through the 2D spectra, except for the susceptibility of the former approach to slit-length-dependent variability in the low-frequency components. The absence of convergence of the low-frequency values of  $S(u,0)$  reflects the peaked nature in the  $v$  direction of the 2D NPS,  $S(u,v)$ , near  $v=0$ . Since the value of  $S_{ss}(u)$  obtained from scanning is scaled by  $L$  to get  $S(u,0)$  [c.f. Eq. (15)], only for values of  $u$  where the addition to the integral of Eq. (14) is proportional to  $L$  will the result be insensitive to changes in  $L$ . Thus, approximating the function  $\text{sinc}^2(Lv)$  as a triangle of base width  $2/L$  and unity height centered at  $v=0$ ,  $S(u,0)$  obtained using a slit length  $L_1$  is approximately equal to that obtained with slit length  $L_2$  only if  $S(u,v)$  is approximately constant in the  $v$  direction between  $v=2/L_1$  and  $v=2/L_2$ . Note that except for  $u=0$ , where  $S(0,v)$  is symmetric about the  $u$  axis, this requirement must also be met between  $v=-2/L_1$  and  $v=-2/L_2$ . Dainty and Shaw have recommended that the slit length be at least equal to the inverse of the frequency resolution (that is, at least equal to the scan distance).<sup>17</sup> Our results indicate that for the digital mammography systems, a length significantly greater than the scan distance may be required for asymptotic convergence of the low-frequency

NPS estimates. In practice, the most direct method of determining sufficiently large  $L$  is probably inspection of cross-sectional cuts through the 2D NPS, obtained at as high a frequency resolution as is practicable, bearing in mind the guidelines of the preceding sentences.

For the noise data studied here, subtraction of a duplicate data set that has been convolved with a two-dimensional rect function kernel is an effective and efficient method for the removal of low-frequency trending effects. The effectiveness of the technique is indicated by the similarity between thick slices extracted from the 2D NPS near the central axes, and on-axis slices (c.f. Fig. 6). 1D spectra obtained from thick slices parallel to the primary axis of interest may not be representative of the on-axis NPS, because the 2D NPS can contain on-axis features not present in adjacent regions of frequency space. For this reason, thin on-axis cuts are recommended.

Algorithms for correction of local detector imperfections, geometric distortions, or sensitivity nonuniformity can either amplify or attenuate components of the NPS. The best and most straightforward way to quantify the noise prior to post-acquisition processing is to obtain noise power spectral estimates from the difference of raw images. Here, raw means as soon as possible after analog-to-digital conversion. When evaluating commercial systems, it may not be possible to obtain data prior to image corrections without assistance from the manufacturer.

It is our opinion that noise power spectral estimates should also be made with images processed using the software correction steps that are to be used in routine practice. Such data are always readily available, and provide the most realistic assessment of noise components present in clinical images. This analysis involves simply calculating spectral estimates from a number of individual processed images, and averaging spectra to reduce the uncertainty in the final estimate. In order to distinguish spectral components that arise from fixed pattern noise that is not fully corrected, these spectra should be compared to those obtained from the same data set, but subtracted from each other pairwise. The latter spectra contain no contributions from fixed pattern noise, since that noise is subtracted out (see Sec. II D 2).

Calculation of an expression for the presampling NPS via cascaded linear systems analysis indicates that the shape of the 1D NPS is governed by three terms. The first term arises from x-ray quantum noise and the phosphor conversion statistics, and is modulated by the system MTF. The second term arises from the Poisson noise associated with the CCD electrons generated by visible photons from the phosphor (secondary quantum noise) and generated thermally. This Poisson noise is modulated only by the pixel sampling aperture function. The third term is the frequency-independent (white) read noise. Comparison of the measured 1D digital spectra with the theoretical presampling spectra shows good agreement for spatial frequencies up to  $\sim 6$  cycles/mm. At higher frequencies, the digital NPS is increasingly larger than the theoretical presampling NPS with increasing frequency. This discrepancy is consistent with aliasing of the NPS components above the Nyquist frequency back into



those between zero frequency and the Nyquist frequency. The aliased noise consists primarily of secondary quantum noise, because the x-ray quantum noise is greatly attenuated by the system MTF above the Nyquist frequency.

## VI. CONCLUSIONS

Fourier analysis has been used to characterize the noise properties of two developmental detectors for digital mammography. The noise power spectra of images from the two systems exhibit several common features. They contain features that are strongly dimension specific, and are often localized to relatively small portions of frequency space. They also contain predominant peaks indicative of periodic additive noise, both on and off the primary frequency axes. On the other hand, the noise properties of the two mammographic detectors differ significantly in some aspects. Over a range of input exposures, the spectra of system 1 are characterized by nearly constant noise power for frequencies greater than about 8 cycles/mm, while those of system 2 exhibit increasingly sharp falloff with increasing frequency. Cuts along the two primary axes of the 2D NPS of system 1 exhibit very different shapes, while those of system 2 are nearly identical along the two axes. At all frequencies, the relative noise of system 2 decreases monotonically with increasing x-ray exposure, while that of system 1 reaches a minimum then begins to increase again. The overall noise of system 2 increases approximately as the square root of the number of x-ray quanta, indicative of x-ray quantum-limited behavior, while that of system 1 increases more slowly, indicating that a significant portion of the noise power arises from sources other than x-ray noise.

The complex nature of the frequency distribution of the noise power in images from digital mammographic systems makes analysis of the complete 2D spectra, rather than only the 1D spectra, important. Straightforward removal of background trending artifacts is possible via a simple filtering process. Cuts obtained along the primary axes of the 2D spectra can provide valid estimates of the 1D NPS without the use of synthetic scanned slit techniques. Spectral estimates from difference images and averaged images can be used to isolate stochastic, fixed pattern, and varying nonstochastic components for identification of noise sources.

Aliasing can contribute significantly to noise power near the Nyquist frequency. Cascaded linear systems analysis is a useful tool for evaluation of the magnitude and sources of aliased noise.

## ACKNOWLEDGMENTS

The authors would like to thank Bob Gagne of the FDA's Center for Devices and Radiological Health for helpful discussions. This work was supported in part by NIH/NCI Grant No. RO1 CA69252.

<sup>a</sup>Electronic mail: mbwilliams@virginia.edu

<sup>1</sup>H. H. Barrett and W. Swindell, *Radiological Imaging: The Theory of Image Formation, Detection, and Processing* (Academic, New York, 1981).

- <sup>2</sup>K. Rossmann, "The spatial frequency spectrum: A means for studying the quality of radiographic imaging systems," *Radiology* **90**, 1-13 (1968).
- <sup>3</sup>J. T. Dobbins, "Effects of undersampling on the proper interpretation of modulation transfer function, noise power spectra, and noise equivalent quanta of digital imaging systems," *Med. Phys.* **22**, 171-181 (1995).
- <sup>4</sup>K. Rossmann, "Spatial fluctuations of x-ray quanta and the recording of radiographic mottle," *Am. J. Roentgenol., Radium Ther. Nucl. Med.* **90**, 863-869 (1963).
- <sup>5</sup>J. H. B. Kemperman and E. A. Trabka, "Exposure fluctuations in model photographic emulsions II. Statistics due to intensifying screens," *Photograph. Sci. Eng.* **25**, 108-111 (1981).
- <sup>6</sup>M. Rabbani, R. Shaw, and R. Van Metter, "Detective quantum efficiency of imaging systems with amplifying and scattering mechanisms," *J. Opt. Soc. Am. A* **4**, 895-901 (1987).
- <sup>7</sup>I. A. Cunningham, M. S. Westmore, and A. Fenster, "Effect of finite detector element width on the spatial frequency dependent detective quantum efficiency," *Proc. SPIE* **2432**, 143-151 (1995).
- <sup>8</sup>R. B. Blackman and J. W. Tukey, *The Measurement of Power Spectra* (Dover, New York, 1958).
- <sup>9</sup>J. M. Sandrik and R. F. Wagner, "Absolute measures of image quality in magnification radiography," *Med. Phys.* **9**, 540-549 (1982).
- <sup>10</sup>I. A. Cunningham and B. K. Reid, "Signal and noise in modulation transfer function determinations using the slit, wire, and edge techniques," *Med. Phys.* **19**, 1037-1044 (1992).
- <sup>11</sup>B. H. Hasegawa, *The Physics of Medical X-ray Imaging*, 2 (Medical Physics, Madison, WI, 1991).
- <sup>12</sup>W. Hillen, U. Schiebel, and T. Zaengel, "Imaging performance of a digital storage phosphor system," *Med. Phys.* **14**, 744-751 (1987).
- <sup>13</sup>H. Roehrig, L. Fajardo, and T. Yu, "Digital x-ray cameras for real time stereotactic breast needle biopsy," *Proc. SPIE* **1896**, 213-224 (1993).
- <sup>14</sup>A. D. A. Y. M. J. Maidment, "Analysis of the spatial-frequency-dependent DQE of optically coupled digital mammography detectors," *Med. Phys.* **21**, 721-729 (1994).
- <sup>15</sup>W. Zhao, I. Blevis, S. Germann, and J. A. Rowlands, "Digital radiography using active matrix readout of amorphous selenium: Construction and evaluation of a prototype real-time detector," *Med. Phys.* **24**, 1834-1843 (1997).
- <sup>16</sup>R. C. Jones, "New method of describing and measuring the granularity of photographic materials," *J. Opt. Soc. Am.* **45**, 799-799 (1955).
- <sup>17</sup>J. C. Dainty and R. Shaw, *Image Science* (Academic, London, 1974).
- <sup>18</sup>J. M. Sandrik and R. F. Wagner, "Radiographic screen-film noise power spectrum: Variation with microdensitometer slit length," *Appl. Opt.* **20**, 2795-2798 (1981).
- <sup>19</sup>K. Koedooder, J. Strackee, and H. W. Venema, "A new method for microdensitometer slit length correction of radiographic noise power spectra," *Med. Phys.* **13**, 469-473 (1986).
- <sup>20</sup>J. T. Dobbins, D. L. Ergun, L. Rutz, D. A. Hinshaw, H. Blume, and D. C. Clark, "DQE(f) of four generations of computed radiography acquisition devices," *Med. Phys.* **22**, 1581-1593 (1995).
- <sup>21</sup>R. L. Jennings, H. Jafroudi, R. M. Gagne, T. R. Fewell, P. W. Quinn, D. E. Steller Artz, J. J. Vucich, M. T. Freedman, and S. K. Mun, "Storage-phosphor-based digital mammography using a low-dose x-ray system optimized for screen-film mammography," *Proc. SPIE* **2708**, 220-232 (1996).
- <sup>22</sup>H. Fujita, D. Tsai, T. Itoh, K. Doi, J. Morishita, K. Ueda, and A. Ohtsuka, "A simple method for determining the modulation transfer function in digital radiography," *IEEE Trans. Med. Imaging* **11**, 34-39 (1992).
- <sup>23</sup>M. L. Giger, K. Doi, and C. E. Metz, "Investigation of basic imaging properties in digital radiography. 2. Noise Wiener spectrum," *Med. Phys.* **11**, 797-805 (1984).
- <sup>24</sup>N. C. Geckinli and C. Yavuz, *Discrete Fourier Transformation and its Application to Power Spectra* (Elsevier, Amsterdam, 1983).
- <sup>25</sup>N. C. Geckinli and C. Yavuz, in *Discrete Fourier Transformation and its Application to Power Spectra* (Elsevier Science, Amsterdam, 1983).
- <sup>26</sup>R. W. Ramirez, *The FFT: Fundamentals and Concepts* (Tektronix, Englewood Cliffs, NJ, 1985).
- <sup>27</sup>J. M. Sandrik and R. F. Wagner, in *The Physics of Medical Imaging: Recording System Measurements and Techniques* (AIP, New York, 1979).
- <sup>28</sup>L. W. Grossman, M. P. Anderson, R. L. Jennings, J. B. Kruger, S. J. Lukes, R. F. Wagner, and C. P. Warr, "Noise analysis of scintillation



- camera images: Stochastic and non-stochastic effects," *Phys. Med. Biol.* **31**, 941-953 (1986).
- <sup>29</sup>W. Shockley and J. R. Pierce, "A theory of noise for electron multipliers," *Proc. Inst. Radio. Eng.* **26**, 321-332 (1938).
- <sup>30</sup>L. Mandel, "Image fluctuations in cascade intensifiers," *Br. J. Appl. Phys.* **10**, 233-234 (1959).
- <sup>31</sup>H. J. Zweig, "Detective quantum efficiency of photographic granularity," *J. Opt. Soc. Am.* **52**, 669-672 (1962).
- <sup>32</sup>I. A. Cunningham, M. S. Westmore, and A. Fenster, "A spatial-frequency dependent quantum accounting diagram and detective quantum efficiency model of signal and noise propagation in cascaded imaging," *Med. Phys.* **21**, 417-427 (1994).
- <sup>33</sup>I. A. Cunningham, M. S. Westmore, and A. Fenster, "Visual impact of the nonzero spatial frequency quantum sink," *Proc. SPIE* **2163**, 274-283 (1994).
- <sup>34</sup>M. B. Williams, P. U. Simoni, L. Smilowitz, M. Stanton, and W. Phillips, "Analysis of the detective quantum efficiency of a developmental detector for digital mammography," *Med. Phys.* (in press).